Cell

Establishing Cerebral Organoids as Models of Human-Specific Brain Evolution

Highlights

- Brain organoids preserve gene expression networks despite elevated metabolic stress

- Chimpanzee organoids enable studies of the evolution of human brain development

- Primary and organoid samples reveal 261 human-specific gene expression changes

- Human radial glia exhibit increased mTOR activation compared to non-human primates

Authors

Alex A. Pollen, Aparna Bhaduri, Madeline G. Andrews, ..., David Haussler, Evan E. Eichler, Arnold R. Kriegstein

Correspondence

alex.pollen@ucsf.edu (A.A.P.),
arnold.kriegstein@ucsf.edu (A.R.K.)

In Brief

Comparisons of cerebral organoids between chimpanzees, macaques, and humans reveal gene duplications and cell-signaling alterations that explain developmental evolutionary differences that are unique to us as a species.

CellPress

Article

Establishing Cerebral Organoids as Models of Human-Specific Brain Evolution

Alex A. Pollen,[1,2,10,11,*] Aparna Bhaduri,[1,2,10] Madeline G. Andrews,[1,2] Tomasz J. Nowakowski,[1,3] Olivia S. Meyerson,[1,2] Mohammed A. Mostajo-Radji,[1,2] Elizabeth Di Lullo,[1,2] Beatriz Alvarado,[1,2] Melanie Bedolli,[1,2] Max L. Dougherty,[4] Ian T. Fiddes,[5] Zev N. Kronenberg,[4] Joe Shuga,[6] Anne A. Leyrat,[6] Jay A. West,[6] Marina Bershteyn,[2] Craig B. Lowe,[7] Bryan J. Pavlovic,[1,2] Sofie R. Salama,[5] David Haussler,[5,8] Evan E. Eichler,[4,9] and Arnold R. Kriegstein[1,2,*]

[1]Department of Neurology, University of California, San Francisco (UCSF), San Francisco, CA, USA
[2]The Eli and Edythe Broad Center of Regeneration Medicine and Stem Cell Research, UCSF, San Francisco, CA, USA
[3]Department of Anatomy, UCSF, San Francisco, CA, USA
[4]Department of Genome Sciences, University of Washington School of Medicine, Seattle, WA, USA
[5]Genomics Institute, University of California, Santa Cruz, Santa Cruz, CA, USA
[6]New Technologies, Fluidigm, South San Francisco, CA, USA
[7]Department of Developmental Biology, Stanford University, Stanford, CA, USA
[8]Howard Hughes Medical Institute, UC Santa Cruz, Santa Cruz, CA, USA
[9]Howard Hughes Medical Institute, University of Washington, Seattle, WA, USA
[10]These authors contributed equally
[11]Lead Contact
*Correspondence: alex.pollen@ucsf.edu (A.A.P.), arnold.kriegstein@ucsf.edu (A.R.K.)
https://doi.org/10.1016/j.cell.2019.01.017

SUMMARY

Direct comparisons of human and non-human primate brains can reveal molecular pathways underlying remarkable specializations of the human brain. However, chimpanzee tissue is inaccessible during neocortical neurogenesis when differences in brain size first appear. To identify human-specific features of cortical development, we leveraged recent innovations that permit generating pluripotent stem cell-derived cerebral organoids from chimpanzee. Despite metabolic differences, organoid models preserve gene regulatory networks related to primary cell types and developmental processes. We further identified 261 differentially expressed genes in human compared to both chimpanzee organoids and macaque cortex, enriched for recent gene duplications, and including multiple regulators of PI3K-AKT-mTOR signaling. We observed increased activation of this pathway in human radial glia, dependent on two receptors upregulated specifically in human: INSR and ITGB8. Our findings establish a platform for systematic analysis of molecular changes contributing to human brain development and evolution.

INTRODUCTION

The 3-fold expansion of the human cerebral cortex is one of the most conspicuous features distinguishing humans from other great apes (Herculano-Houzel, 2012). This size difference is already apparent during early cortical development at mid-gestation, prior to the completion of neurogenesis (Sakai et al., 2012). Long-standing models propose that increased numbers

of neural stem and progenitor cells could account for human brain expansion (Rakic, 1995). Radial glia act as neural stem cells to generate excitatory neurons of the cerebral cortex (Noctor et al., 2001), and recent comparative studies suggest a cell-intrinsic increase in proliferative divisions among radial glia as a candidate mechanism for human brain expansion (Otani et al., 2016). Nonetheless, the molecular basis for differences in developmental cell behavior remains poorly understood because primary brain tissue is largely inaccessible from chimpanzees, our closest living relatives, during developmental stages in which neurons of the cortex are generated.

Induced pluripotent stem cells (iPSCs) derived from great apes provide a platform for experimentally addressing how human-specific genetic changes differentially affect aspects of development (Blake et al., 2018; Gallego Romero et al., 2015; Marchetto et al., 2013; Pavlovic et al., 2018; Prescott et al., 2015; Silver, 2016). Organoid models derived from pluripotent stem cells harness natural properties of self-assembly to mimic early developmental processes across diverse tissues (Eiraku et al., 2008, 2011; Clevers, 2016). Recent studies have begun to compare gene expression between human and chimpanzee cerebral organoids from a limited number of individuals (Mora-Bermúdez et al., 2016), but systematic quantitative comparisons across multiple individuals and time points are required to distinguish species differences from individual differences. Additionally, primate outgroups beyond chimpanzee are necessary to determine which evolutionary changes are derived in the human lineage. Similarly, analysis of the fidelity of organoid models to primary tissue requires comparing key sources of biological and technical variation across a range of protocols and individuals.

Single-cell RNA sequencing provides an opportunity to compare gene expression in homologous cell types between primary tissue and organoid models and across species (Pollen et al., 2014; Camp et al., 2015). Although developing tissue and organoid models contain a diversity of cell types, new
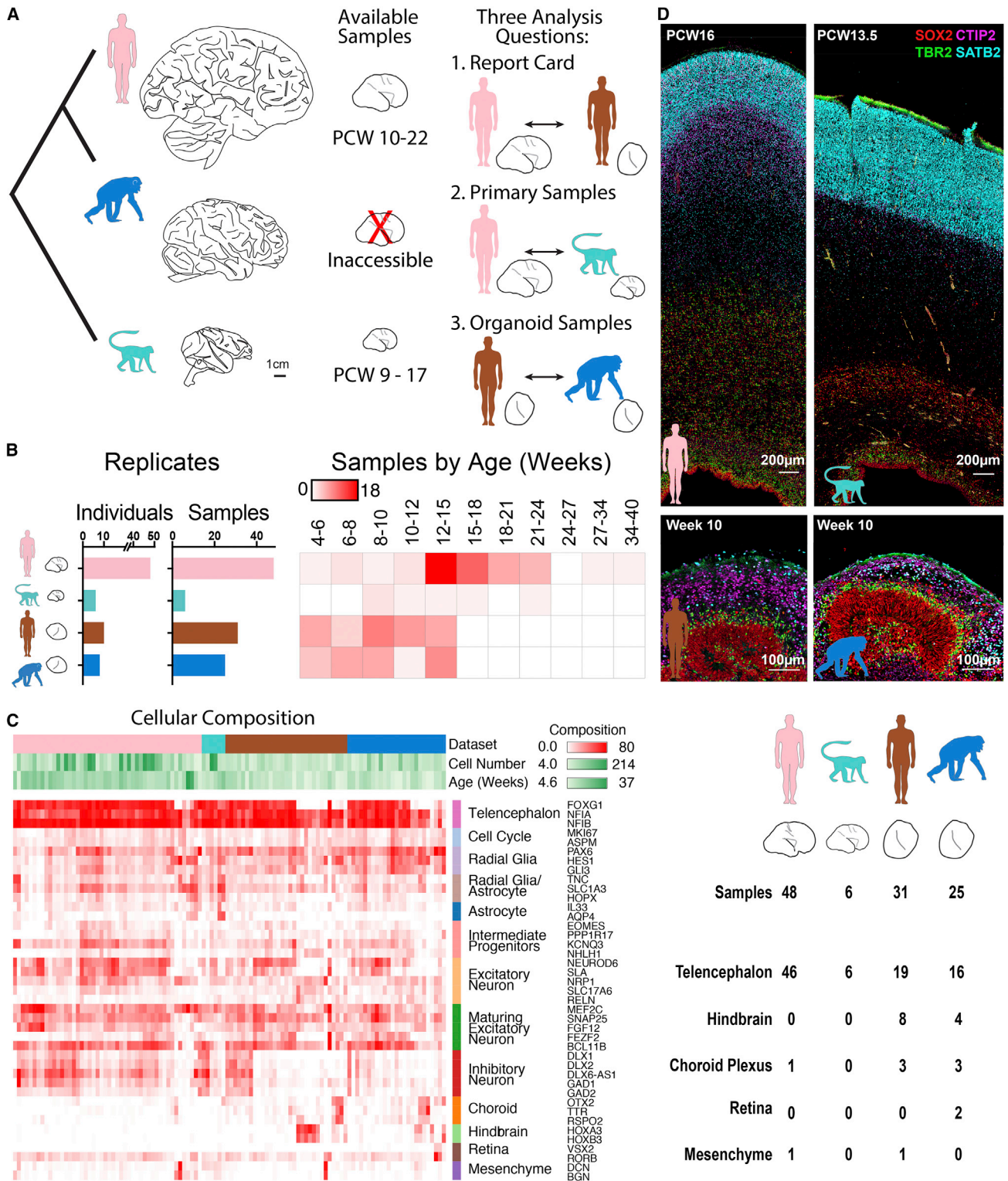
Figure 1. Organoid Models Reflect Normal Features of Human and Chimpanzee Brain Development

(A) The human brain has expanded dramatically compared with other primates, but brain tissue is largely inaccessible from developing chimpanzee. To compare human and chimpanzee development, our study focuses on three analysis questions that integrate data from primary human (pink) and macaque (light blue) samples with human (brown) and chimpanzee (blue) organoid models.

(legend continued on next page)

analysis methods allow for the identification of homologous cell types and gene regulatory networks based on the expression of thousands of genes in single cells (Butler et al., 2018; Nowakowski et al., 2017). Here, we use single-cell gene expression comparisons across the span of cortical neurogenesis to undertake three analyses that together enable the study of gene regulatory evolution during human brain development (Figure 1A). First, we examine the extent to which cell types, gene co-expression patterns, and developmental trajectories from primary tissue samples are preserved in organoid models. Second, we explore how gene expression patterns diverge between human and macaque during cortical development using primary tissue. Finally, we analyze which of the expression differences between human and macaque emerged along the human lineage in the last six million years using human and chimpanzee organoid models that give us an otherwise inaccessible window into patterns of early brain development in our closest living relative.

We find that organoid models preserve the vast majority of gene co-expression patterns observed in primary tissue during cortical development, supporting the utility of these models for studying the evolution of gene regulation. Nonetheless, across commonly used protocols, organoid models display a heterogeneous composition and upregulation of glycolysis, endoplasmic reticulum stress, and electron transport pathways, isolating potentially important differences with primary tissue, while also highlighting avenues for further improving this useful model. Similarly, we find striking conservation of gene networks across human, chimpanzee, and macaque. However, we also identify a common set of 261 genes that are differentially expressed between human and macaque primary cortical cells and between human and chimpanzee organoid cells. These candidate human-specific gene expression differences are largely distinct from those reported in fibroblasts and pluripotent stem cells (Gallego Romero et al., 2015) and include many genes overlapping recent segmental duplications. Interestingly, we find increased activation of the PI3K/AKT/mTOR pathway specifically in human outer subventricular zone radial glia. Across species, radial glia are particularly sensitive to perturbations in this pathway compared with other cell types, and we show that pS6 activation in human depends in part on two genes, INSR and ITGB8, that are upregulated in the human lineage, suggesting a molecular mechanism that may contribute to human-specific changes in neural stem cell behavior.

RESULTS

Cell Diversity in Primary Samples and Organoid Models
Cortical development involves the emergence of diverse communities of cells, including excitatory neuron lineage cells (radial glia, intermediate progenitor cells, excitatory neurons), inhibitory neurons that migrate to the cortex from the ventral telencephalon, glial cells (astrocytes, oligodendrocytes, and microglia), and vascular cells. Organoid models may capture a subset of these cell types while also introducing additional sources of variation in cell types, cell states, and gene expression (Quadrato et al., 2017). We reasoned that single-cell gene expression would allow us to evaluate the extent to which cell types, gene regulatory networks, and developmental trajectories are preserved in organoid models. Therefore, we designed a large-scale experiment to compare single-cell gene expression using a standardized protocol across primary tissue from 48 human samples (Nowakowski et al., 2017) and 6 macaque samples with 56 organoids derived from 10 human and 8 chimpanzee individuals, distributed across stages of cortical neurogenesis (Figure 1B; Tables S1 and S2). We generated organoids based on a protocol developed in the Sasai lab (Kadoshima et al., 2013), and we further analyzed published single-cell gene expression data from two other organoid protocols representing a continuum of guided to unguided patterning (Camp et al., 2015; Lancaster et al., 2013; Sloan et al., 2017) (Figure S1). To analyze the largest number of homologous genes across human, chimpanzee, and macaque, we updated gene models and orthology assignments in both chimpanzee and macaque genomes using the comparative annotation toolkit (Fiddes et al., 2018), providing a more accurate and comparable estimate of gene expression levels between species. In addition, we recently improved the contiguity of the chimpanzee genome through *de novo* assembly, increasing alignment rates (Kronenberg et al., 2018). Using these improvements, we were able to align reads to each species' native genome and examine gene expression across 49,360 orthologous genes (Figure S1). The number of genes detected per cell was comparable in human and chimpanzee organoids, but slightly lower in macaque, indicating that expression values may be underestimated for some macaque genes (Figure S1).

To characterize the cellular heterogeneity of organoid models, we first analyzed the frequency of cells expressing marker genes for cortical cell types as well as for common off-target lineages. The majority of human and chimpanzee organoids expressed markers of telencephalic regional identity, including cortical excitatory lineage cells, and a subset of inhibitory neurons from ventral telencephalon (Figures 1C and S1). A minority of organoids predominantly contained off-target lineages, including hindbrain, choroid plexus, retina, and mesenchymal cells, with a few individuals mainly accounting for the bias in differentiation potential (Figures S1 and S2). For example, iPSC lines from two human individuals repeatedly produced off-target, largely hindbrain cells (8/9 organoids), while the other eight human individuals mainly produced telencephalon cells (18/22 organoids). Nonetheless,

(B) Histograms and heatmap depict the number of individuals and primary or organoid samples and the distribution of samples over post conception or post differentiation weeks.

(C) Heatmap represents the fraction of cells expressing each marker gene across cells from each primary sample or organoid, and the table summarizes the number of samples that predominantly express markers for a given regional identity.

(D) Immunohistochemistry for markers of radial glia (SOX2), intermediate progenitors TBR2 (EOMES), and neurons CTIP2 (BCL11B) and SATB2, reveals histological and cellular features of normal neurogenesis in the germinal zones of human and chimpanzee cerebral organoids, but a much more extensive intermediate zone and cortical plate in primary samples.

See also Figure S1 and Table S1.
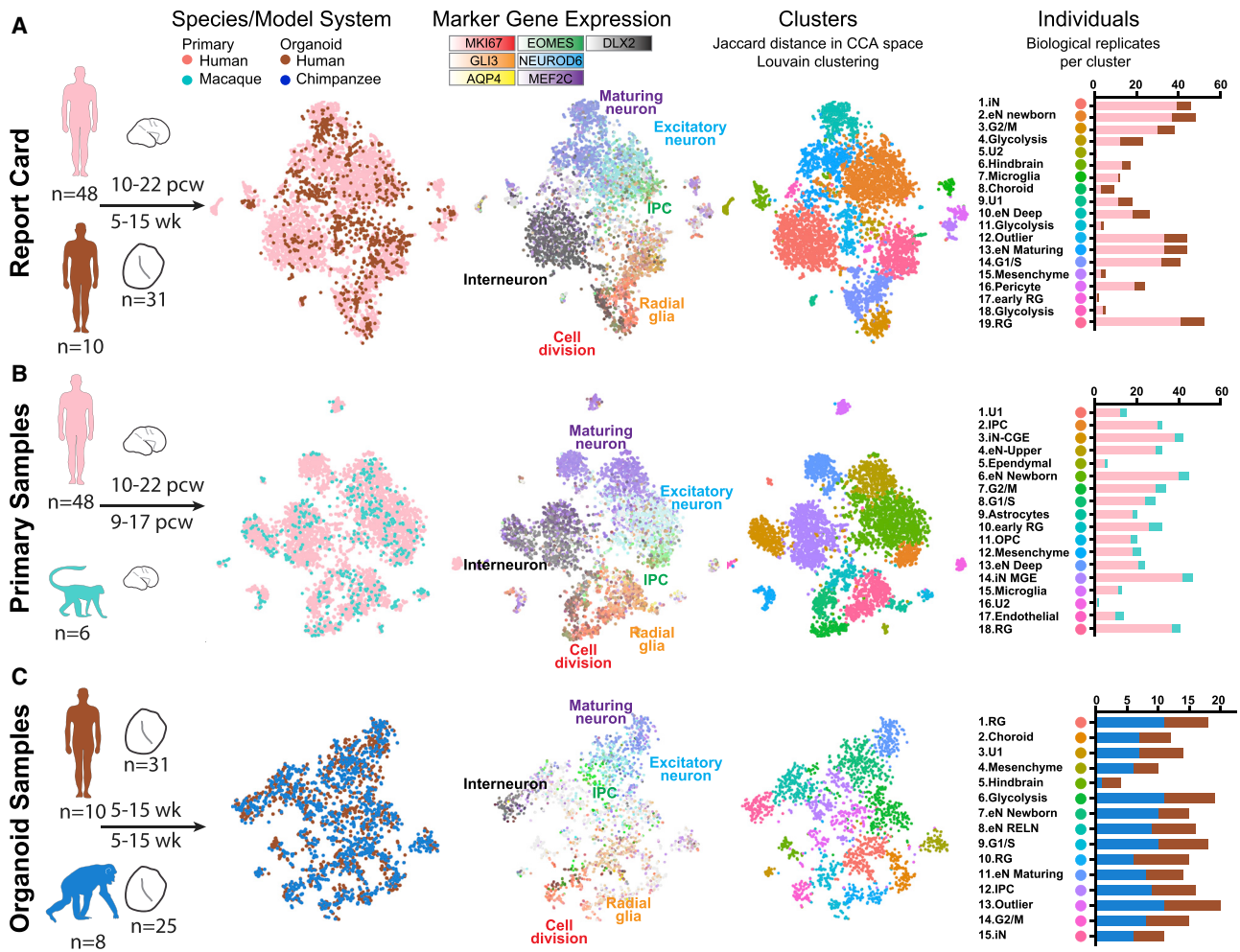
Figure 2. Identification of Homologous Cell Types across Species and Model System

(A–C) Pairwise comparisons of human primary and human organoid cells (A), human primary and macaque primary cells (B), and human organoid and chimpanzee organoid cells (C), with developmental stages and the number of distinct individuals and organoids depicted under the schematics. Columns 1–3 display cells plotted based on gene expression similarity after principle components analysis and t-stochastic neighbor embedding, and colored by species or model system (column 1), by marker genes for known cell types (column 2), and by clusters following Louvain-Jaccard clustering (column 3). Column 4 indicates the number of primary individuals or distinct iPSC lines contributing to each cluster.

See also Figure S2 and Table S2.

among telencephalon organoids, we observed additional variation in the proportion of excitatory and inhibitory neurons, indicating experimental variation in composition (Figure 1C). To further compare the cellular heterogeneity of primary cortical tissue and organoids, we performed immunohistochemistry for proteins that label radial glia and excitatory neurons. The human and macaque primary cortex samples displayed clear organization of radial glia and intermediate progenitors in the ventricular and subventricular zones and neurons migrating toward the cortical plate over an extensive intermediate zone. Similarly, cortical-like organoids from both human and chimpanzee contained ventricular and subventricular zone-like structures in which cells expressed markers of radial glia and intermediate progenitors (Figure 1D). Outside of these zones, we observed cells expressing deep and upper layer markers at 6 and 15 weeks of organoid differentiation, respectively (Figures 1D and S1), but the overall distance

from the ventricle to the periphery was greatly compressed compared to primary samples. Thus, organoid models contained cell types and histological features reflective of cortical germinal zones but demonstrated restricted structural organization and varied in composition across experiments.

We next sought to define homologous cell types across model systems and species. Although all cells were dissociated and captured using a common protocol, biological and technical differences across primary and organoid cells and between species create challenges for unbiased clustering of combined datasets (Figure S2). To overcome this limitation, we performed canonical correlation analysis (Butler et al., 2018), which finds common sources of variation across datasets, to co-cluster cells from different model systems in three pairwise comparisons. For the organoid report card analysis, we co-clustered human primary and human organoid cells (Figure 2A). For the

comparative analysis in primary tissue samples, we co-clustered human and macaque primary cells (Figure 2B), and for the comparative analysis in organoid samples, we co-clustered human and chimpanzee cells (Figure 2C). In each case, we identified major telencephalic cell types including radial glia across cell-cycle phases, intermediate progenitor cells, excitatory neurons at different stages of maturation, and inhibitory neurons. These cell types were present across model systems and species and repeatedly emerged across individuals and with alternative co-clustering methods (Figures 2A–2C and S2). In addition, most individuals contributed to most clusters, indicating that cell type and state drove clustering rather than individual or species (Figure S2). Interestingly, the overall cell composition was highly similar across species in both the primary sample comparison of human and macaque and the organoid comparison of human and chimpanzee. However, human primary samples and human organoids differed in composition, with primary telencephalon samples containing a greater proportion of interneurons, and organoids containing a greater proportion of radial glia and glycolytic cells (Figure S2). Together, these analyses provided a baseline for comparing cells of the same type across model systems and species.

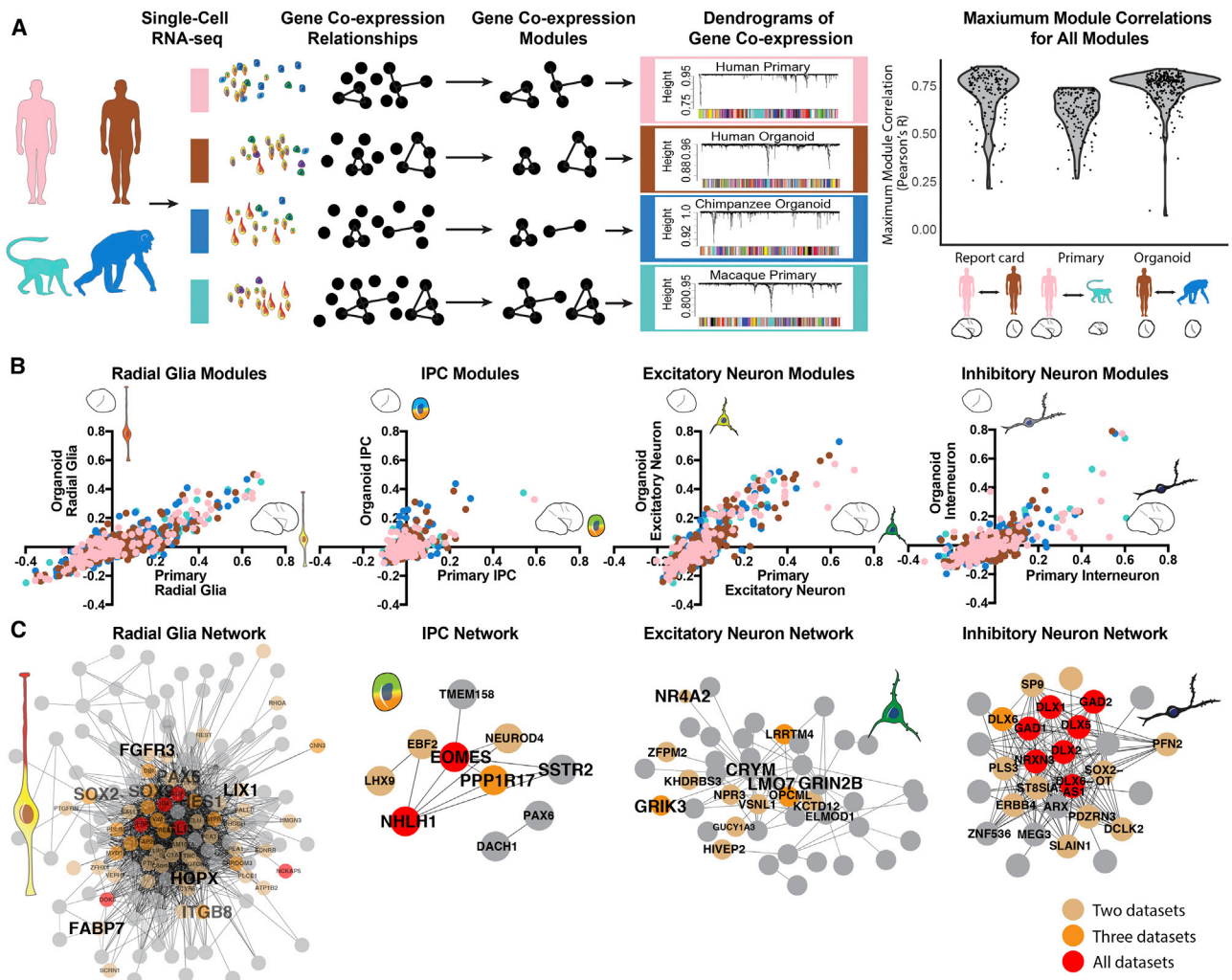## Preservation and Conservation of Gene Co-expression Patterns

Gene co-expression relationships often reflect biological processes related to cell type, cell state, and signaling pathways, in which many genes with related functions are coordinately regulated (Oldham et al., 2008; Langfelder and Horvath, 2008). To identify gene co-expression relationships, we performed weighted gene correlation network analysis (WGCNA) separately in each dataset (Figure 3A). Importantly, gene co-expression relationships can be determined independently from cell-clustering results, providing an additional method for comparing datasets. We applied this approach to examine the extent to which gene co-expression modules are preserved between primary samples and organoid models and conserved across species by separately determining gene co-expression relationships in all primary human cells, all primary macaque cells, all human organoid cells, and all chimpanzee organoid cells (Tables S3 and S4). Despite variation in cell composition, we found that the majority of co-expression modules derived independently in each dataset were highly correlated (Pearson's R > 0.5) (Figures 3A and S3). For example, over 70% of human primary modules showed a Pearson's correlation greater than 0.7 with a human organoid module. Overall, the shared patterns of co-expression provided systematic evidence for preserved gene regulatory mechanisms in organoid models and conservation of these regulatory relationships across species.

We next examined whether these co-expression modules related to common biological processes. Using a general linear model, we identified many modules related to cell type as independently defined by homologous clustering, but relatively few modules related to differences between individuals, between the organoid model system and primary samples, or between species (Figure S3). For example, many modules generated in each dataset correlated with radial glia and excitatory neuron clusters, while a subset correlated with intermediate progenitor and interneuron subtypes (Figure 3B). These relationships allowed us to generate consensus modules related to cell type that emerge across all datasets (Figure 3C). Notably, individual modules related to finer aspects of cell subtype variation than could be discerned from the cell-type clustering. For example modules correlated with radial glia cell identity included networks related to young radial glia (organoid.chimp.ME.lavenderblush3: *LIX1*, *HMGA2*), outer subventricular zone radial glia (primary.human.ME.palevioletred: *HOPX*, *SLCO1C1*, *MOXD1*, *S1PR1*), and mature radial glia (primary.human.ME.magenta: *CLU*, *ATP1A2*, *TNC* (Table S4). Similarly, modules correlated with inhibitory neurons included networks related to lateral ganglionic eminence (LGE)- and caudal ganglionic eminence (CGE)-derived (e.g., primary.human.ME.antiquewhite2: *PROX1*, *SCGN*, *CALB2*, *SP8*) and medial ganglionic eminence (MGE)-derived (primary.human.ME.yellow3: *MAF*, *LHX6*, *SST*) interneuron subtypes, with organoids enriched for LGE-derived interneuron subtypes (Figure S3). In addition, highly correlated modules that related to cell states independently emerged in all four datasets, including the G2/M and G1/S transitions and excitatory neuron maturation (Figure S3). On the other hand, modules related to cell types not commonly found in organoids, such as microglia, and oligodendrocyte precursors, emerged across species, but only in primary cell datasets (Figure S3). The independent emergence of modules highly correlated to cell type indicates that transcriptional programs determining cell types are largely conserved among primates and that gene regulatory mechanisms in major telencephalic cell types and states can be modeled in cerebral organoids.

Developmental Processes and Metabolic States

We further examined the extent to which organoid models preserve developmental trajectories related to neuronal differentiation, radial glia maturation, and cortical areal identity that we recently described during normal cortical development (Nowakowski et al., 2017). As previously reported, the signature of differentiation from radial glia to excitatory neurons is highly correlated between primary cells and organoid models, with very few genes deviating from the *in vivo* trajectory (Figure 4A) (Camp et al., 2015). We similarly found that gene co-expression modules representing radial glia maturation independently arose in primary and organoid radial glia datasets (Figures 4B and S4). In addition, astrocyte production was restricted to the oldest organoid samples (Figure S4) as recently reported (Sloan et al., 2017). However, the radial glia maturation signature was more strongly correlated with primary sample age than with organoid age, indicating variability in the timing of organoid maturation (Figure 4B). The emergence of distinct cortical areas is a major feature of normal cortical development, and maturing excitatory neurons show transcriptional signatures of areal identity. Therefore, we used excitatory neurons from human primary visual (V1) and prefrontal cortex (PFC) to construct a classifier for areal identity (Figure 4C). Consistent with previous immunohistochemical observations of gradients in several regional identity genes (Eiraku et al., 2008; Kadoshima et al., 2013), most organoids contained a mixture of V1-like and PFC-like excitatory neurons and additional neurons of unknown areal identity (Figure 4C). Overall, neuronal differentiation, radial glia maturation, and aspects of cortical arealization occurred spontaneously in

Figure 3. Conservation of Gene Co-expression Modules across Species and Model System

(A) Gene co-expression relationships were determined independently in each dataset using WGCNA. Violin plots indicate the distribution of maximum correlation values for all co-expression modules in each pairwise comparison.
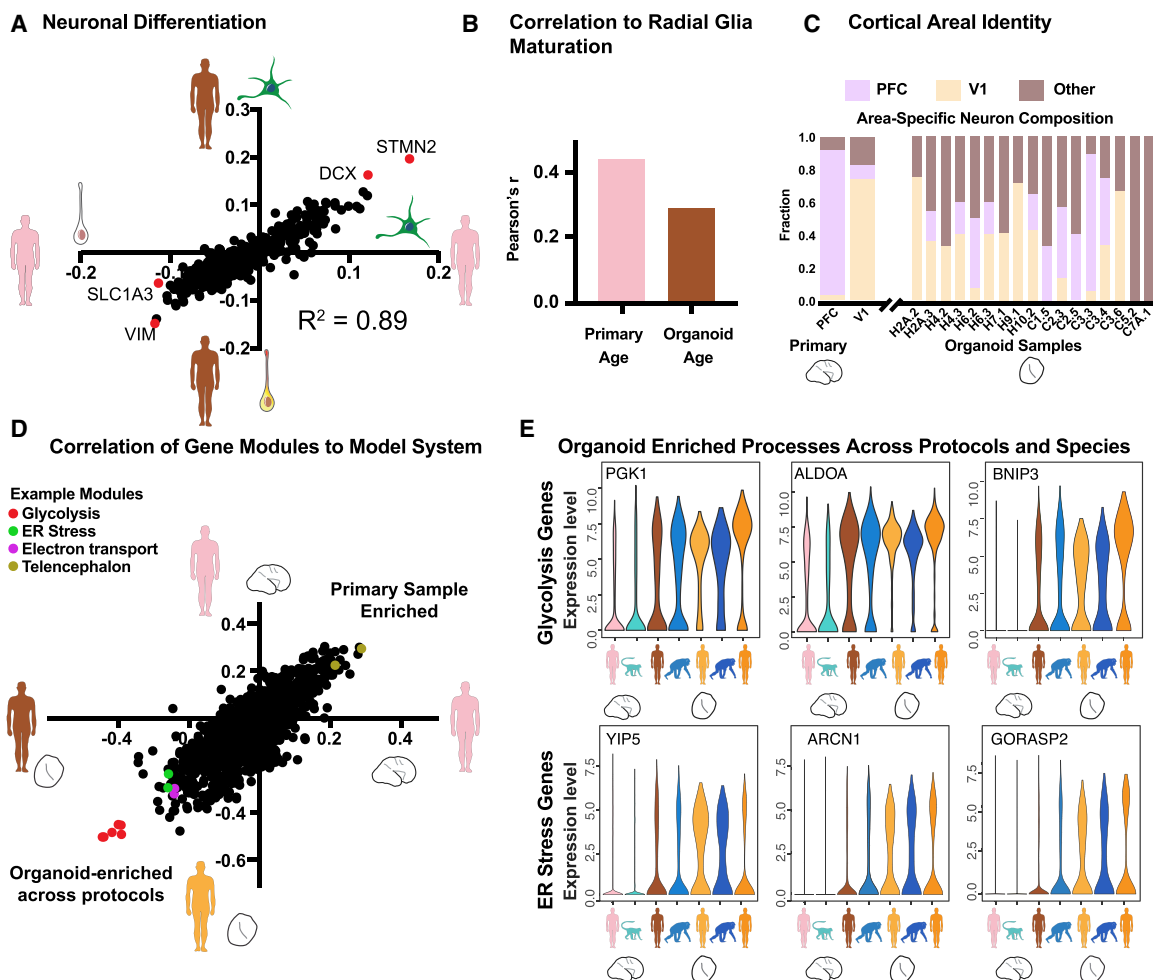
(B) Scatterplots depict the correlation of modules to cell types independently determined in organoid (y axis) and primary cell datasets (x axis). Notably many modules correlate to coarse cell-type classifications, representing finer cell subtypes and states. Dots are colored by the model system in which the network was identified.

(C) Network maps depict the correlation of genes from top cell type networks across all four datasets. Edges represent a correlation with R > 0.25, with edge length inversely related to correlation strength. Brown, orange, and red dots highlight genes that appear in the core module for 2, 3, and 4 networks respectively. See also Figure S3 and Tables S3, S4, and S5.

organoid models, but the timing of radial glia maturation and arealization of neuronal identity was heterogeneous.

We next explored the biological processes that were strongly associated with organoid models when compared to primary cells. We hypothesized that differences resulting from the organoid system might be reflected across a range of cerebral organoid protocols and might illuminate general opportunities for improving these culture systems. Indeed, we found that three independent organoid protocols varying in their use of patterning molecules to constrain regionalization displayed upregulation of the same gene co-expression modules compared with primary samples (Figures 4D and S4). In particular, the modules with strongest organoid enrichment across protocols related to

glycolysis (Figures 4D and S4). Interestingly, similar glycolysis gene co-expression modules emerged in primary human and primary macaque cells, but the expression of genes in these modules was higher and more pervasive in organoid cells (Figure 4E), indicating over-activation of a normal metabolic pathway. In addition, we observed enrichment in organoids for modules involving endoplasmic reticulum stress, including the unfolded protein response pathway and electron transport (Figures 4E and S5). In contrast, modules enriched in primary samples related to telencephalon regional identity and excitatory neuron subtypes that were also commonly observed in organoids but were found at a higher frequency in primary samples (Figure 4D). Overall, current organoid models preserve gene co-expression networks and

Figure 4. Organoid Modules Recapitulate Developmental Gene Expression Trajectories but Exhibit Elevated Metabolic Stress across Protocols

(A) Scatterplot shows the correlation of genes to the neuronal differentiation signature as derived in organoids (y axis) and in primary cells (x axis).

(B) Histogram of R values indicating the correlation of the radial glia maturation network to sample age across primary radial glia (PCW8-22) and organoid radial glia (Week 5–15).

(C) Areal identity of maturing excitatory neurons in primary tissue and across organoids as predicted by a classifier. First two columns indicate primary cells with known areal identity.

(D) Scatterplot shows the correlation of all gene co-expression modules to primary human cells (positive on both axes) versus organoid cells from this paper using the Kadoshima protocol (negative on x axis) and a previous paper (Camp et al., 2015) using a whole-brain organoid protocol (negative on y axis). Modules are generated independently in each dataset and correlated to primary or organoid cell identity. Glycolysis, endoplasmic-reticulum (ER) stress, and electron transport modules show a strong correlation with organoid cells from both protocols.

(E) Violin plots illustrate the distribution of single-cell gene expression values for hub genes in the glycolysis and ER stress co-expression modules from primary human and macaque cells (columns 1 and 2) organoid cells generated in this paper using the Kadoshima protocol (columns 3 and 4), organoid cells generated using a whole-brain organoid protocol (columns 5 and 6; Camp et al., 2015; Mora-Bermúdez et al., 2016), and a cortical spheroid protocol (column 7; Sloan et al., 2017).

See also Figure S4.

developmental trajectories observed in primary tissue, while our analysis highlights specific targets for optimization of future organoid culture systems, including upregulated metabolic stress pathways, impoverished cortical architecture, and the variability of cell composition across differentiation experiments (Figure S4).

Human-Specific Gene Expression Changes

The preservation of gene regulatory networks and developmental processes in organoid models allowed us to search for gene expression patterns that evolved in the last six million years. Our strategy involved first comparing primary human and primary macaque cortex to identify gene expression differences that occur during normal development across more distant primates. Next, to identify which of these changes occurred in recent evolution, we compared gene expression in human and chimpanzee organoid models. We used a likelihood ratio test (LRT) commonly applied to single-cell gene expression data and a general linear model to calculate differential
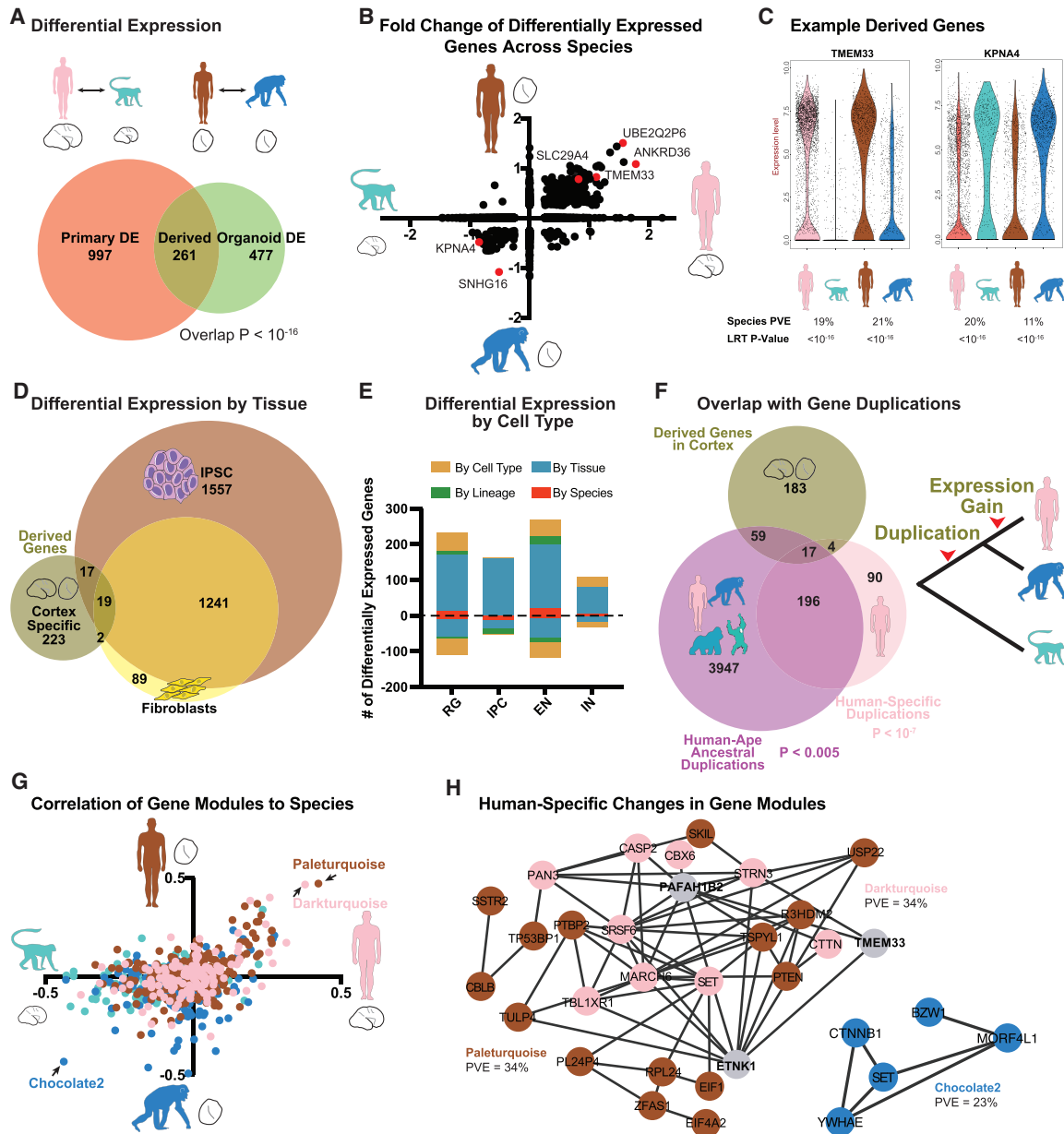
Figure 5. Human-Specific Gene Expression Patterns during Cortical Neurogenesis

(A) Venn diagram represents the number of differentially expressed genes between primary human and macaque (left circle) and differentially expressed genes between human and chimpanzee organoids with cortical identity (LRT adjusted p value <0.0005). Overlap represents candidate genes with human-specific regulatory changes.

(B) Scatterplot illustrates the fold change for genes differentially expressed in either primary cell or organoid cell comparisons across all cells.

(C) Violin plots for genes up- or downregulated specifically in human cells.

(D) Venn diagram represents the overlap between derived regulatory changes in cortex and human and chimpanzee differential expression previously determined in fibroblasts and iPSCs (Gallego Romero et al., 2015).

(E) Histogram highlights the number of derived expression changes that are shared across cortex, iPSC, and fibroblasts (by species, red), found only in cortex (by tissue, blue), found only in the excitatory neuron lineage of radial glia, intermediate progenitor cells (IPCs), and excitatory neurons (by lineage, green), or found in one cortical cell type (by cell type, dark yellow).

(F) Venn diagram represents the overlap between derived genes in cortex, and genes with duplications or copy number expansions that are human specific (pink) or occurred in apes along the lineage leading to humans, prior to our divergence with chimpanzee (purple) (Sudmant et al., 2013). Note that some genes underwent multiple duplication events along the human lineage (overlap between pink and purple circles).

(legend continued on next page)

expression, accounting for a large number of technical and biological replicates (STAR Methods; Table S5). Across cells from primary telencephalon samples, we observed 1,258 differentially expressed genes between human and macaque, and across cells from organoids with a telencephalon identity, we observed 738 differentially expressed genes between human and chimpanzee (Figures 5A and S6). The fold change and direction of these differentially expressed genes was correlated (Figures 5B and 5C) and 261 genes overlapped across comparisons ($p < 10^{-16}$), providing a set of candidate genes independently supported by primary tissue and organoid comparisons that are likely to have derived human-specific gene expression patterns during cortical development.

We further examined the properties of derived genes with respect to the specificity of differential expression and the overlap with genes underlying neurodevelopmental disorders. To examine the specificity of gene expression changes, we compared our results in developing cortex with recent studies in human and chimpanzee fibroblasts and iPSCs (Gallego Romero et al., 2015). Of the 261 candidate derived gene expression changes, 85% were specific to cortical development (Figures 5D and S5). Nonetheless, these differences were frequently shared across cortical cell types (Figures 5E and S5). Because genes linked to autism spectrum disorder also show enriched expression in the stages and cell types of cortical development that we surveyed (Bakken et al., 2016), we examined whether derived regulatory changes included disease-linked genes. Of 78 genes with an excess of *de novo* mutations in autism (Stessman et al., 2017), five overlapped with the stringent set of 261 derived changes on the human lineage, and an additional four overlapped with a broader set of 668 genes differentially expressed in at least one cortical cell type (Figure 5E), including *SRCAP*, which also showed broad species differences by *in situ* hybridization (Figure S5). These overlaps were both moderately significant against the background set of all detected genes (hypergeometric $p < 0.005$.) Thus, our approach of combining primary sample and organoid comparisons revealed many candidate tissue-specific gene expression patterns during human brain development, and highlighted examples of disease-related genes that may have human-specific developmental functions.

Recent studies have identified human-specific genetic changes likely to influence gene regulation or gene copy number (Dennis et al., 2012; McLean et al., 2011; Pollard et al., 2006; Charrier et al., 2012; Dennis et al., 2017). By overlapping major classes of structural genomic changes with human-specific gene expression differences, we sought to identify candidate sequence changes particularly likely to influence gene expression during cortical development. We found that recently duplicated genes (Sudmant et al., 2013) were significantly over-represented among differentially expressed genes (Figure 5F; $p < 10^{-7}$). For example, nearly all genes in the *SMN1* and *ARL17A* loci showed increased expression in human developing cortex compared to chimpanzee and macaque (Figure S5). This is perhaps unsurprising as the human genome contains additional copies of these duplicated genes. Nonetheless, human-specific duplications may also result in daughter genes with new expression patterns (Dennis et al., 2017). For example, the NPIP family has expanded in copy number in the ape and human lineage (Johnson et al., 2001), but only a single human paralog, *NPIPB5*, shows derived regulatory changes in cortical tissue (Table S6). Duplications that occurred earlier in ape evolution may also provide a substrate for additional regulatory changes (Dennis et al., 2017; Ohno, 1970). Therefore, we examined whether duplications that occurred in the human lineage prior to our divergence from chimpanzee were also enriched among derived regulatory changes. Overall, we found a modest enrichment for differential expression among these older duplication events ($p < 0.005$). These include intriguing examples, such as the monoamine transporter *SLC29A4*, which appears to have duplicated in the common ancestor of human and chimpanzee but is more highly expressed in human cortical development, particularly in a subset of intermediate zone and cortical plate cells (Figures 5F and S5).

Models of regulatory evolution suggest that genetic changes influencing hub genes may increase the expression of species-specific regulatory networks. To identify gene networks that changed together in the human lineage through the influence of common regulatory mechanisms, we further analyzed whether gene co-expression modules showed human-specific expression patterns. We found that many co-expression modules enriched in primary human compared with primary macaque samples were also upregulated in human organoid compared with chimpanzee organoid samples, suggesting human-specific regulation of these networks (Figure 5G). The two strongest modules with a derived gain of expression in the human lineage were enriched for negative regulation of transcription related to G1/S transition and neuronal apoptosis ($p < 10^{-6}$). In addition, several modules with derived expression changes along the human lineage also showed enrichment for particular cell types (Table S4). These modules with species and cell-type enrichment included primary.human.ME.darkred, whose upregulation in human radial glia may be partly driven by duplication of NBPF genes, and organoid.human.ME.skyblue4 that was downregulated in human excitatory neurons and contained genes related to axonal fasciculation. Together, these results provide candidate regulatory networks that may have evolved together through coordinated transcriptional changes.

Radial glia are particularly likely to influence the evolutionary expansion of the brain (Noctor et al., 2001; Rakic, 2003), and we next examined whether differentially expressed pathways might influence radial glial development. We did not observe significant gene ontology enrichment among differentially expressed genes after multiple hypothesis correction, but genes in the PI3K-AKT-mTOR pathway appeared in the top-ranked categories (e.g., FOXO3 signaling $p = 0.065$, Figures 6A and

(G) Scatterplot illustrates the correlation of each gene co-expression module to species across primary cells (x axis) and organoid cells (y axis). Colors correspond to the dataset in which the module was generated.

(H) Network maps highlight genes from the modules with expression most correlated to human or primate cell sources. Edges correspond to a correlation R > 0.25.

See also Figure S5 and Table S6.
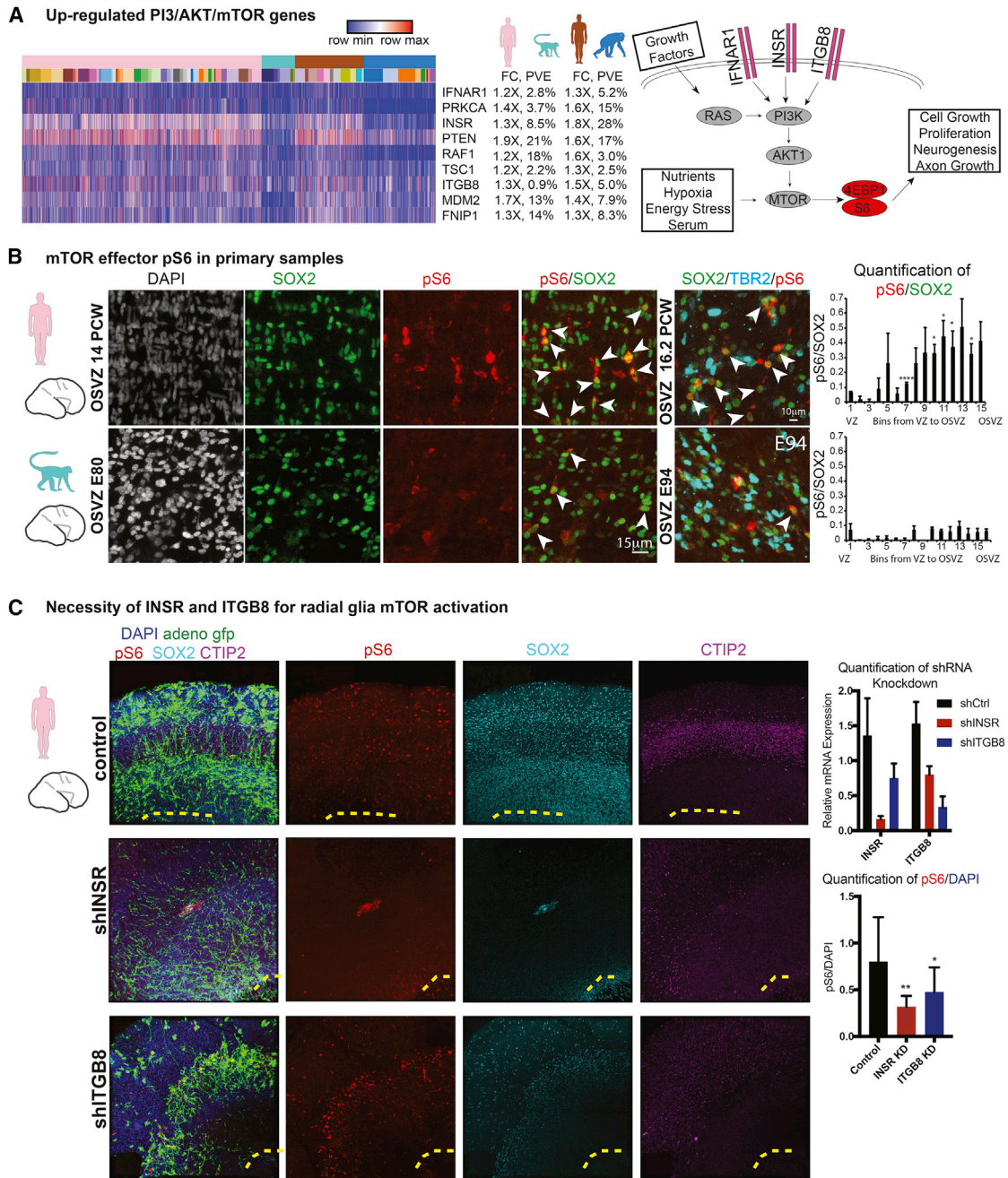
Figure 6. Human Outer Subventricular Zone Radial Glia Show Increased Phosphorylation of the mTOR Effector S6 Compared to Other Primates

(A) Heatmap across all cells (columns) illustrating differential expression for a subset genes related to the PI3K-AKT-mTOR pathway, with label showing the log$_2$(fold change) and percentage of variance explained by species in both the primary cell and the organoid cell comparison. Schematic highlights receptors upregulated in human and their relationship to downstream effectors, phosphorylated S6 (pS6), and phosphorylated 4EBP1 (p4EBP1).

(B) Immunohistochemistry illustrates abundant labeling of pS6 in radial glia of primary human outer subventricular zone compared to primary macaque. Quantification of the levels of pS6 is shown in equal bins across the ventricular and outer subventricular zone. Significant upregulation in human compared to macaque with *p < 0.05 or ****p < 0.0001 in each bin, with aggregated results across bins significant at p < 10^{-6} (Welch's t test).

(C) Immunohistochemistry in human slice culture (representative example, n = 4) shows the fiber architecture (adeno GFP), pS6, SOX2 (progenitor population), and CTIP2 (neuronal population) in slices treated with hairpins targeting INSR or ITGB8. Quantification of knockdown and pS6 levels in outer subventricular zone is also shown. Note the control sample also contains pS6 in the cortical plate as previously observed. Significant downregulation of pS6 levels with *p < 0.05 or **p < 0.01 (Welch's t test).

See also Figure S6.

S6; Table S6). Further analysis of mTOR pathway genes revealed that both activators (INSR, ITGB8, IFNAR1) and repressors (PTEN) showed strong upregulation in human organoids and human primary cells. Although this pathway is known to influence neuronal maturation, we recently observed strong immunoreactivity for the mTOR effector phosphorylated ribosomal protein S6 (pS6) in outersubventricular zone radial glia (Nowakowski et al., 2017). To determine whether patterns of mTOR activation changed in radial glia during recent human evolution, we first performed immunohistochemistry for pS6 across species using an antibody to conserved phosphorylation sites. We observed comparable levels of immunoreactivity among neurons in human and macaque cortical plate (Figure S6). However, in germinal zones, we found that pS6 strongly labeled human primary and organoid radial glial cells, in particular, those away from the ventricle and ventricular zone-like regions (Figures 6B, 6C, and S6). Conversely, staining in primary macaque and chimpanzee organoid sections showed less pervasive and fainter pS6 immunoreactivity than in human radial glia (Figures 6B, 6C, and S6), suggesting that changes in the activity of the mTOR signaling pathway have evolved recently in human outer radial glia.

We next sought to further quantify changes in mTOR activation across species. Because many components of this pathway undergo post-translational regulation, we performed western blots for INSR and the phosphorylated mTOR effectors S6, 4EBP1, and NRDG1. To enrich for progenitor cells, we cultured primary human and macaque cells for several passages in media that favors progenitors (Onorati et al., 2016), and we examined 5-week-old organoids that contain a high proportion of progenitors. We found that the candidate upstream factor INSR was upregulated at the protein level commensurate with expression differences determined by single-cell RNA sequencing (Figure S6). In addition, pS6, p4EBP1, and pNRDG1 all showed increased abundance in human cells compared with chimpanzee organoid and primary macaque cells, consistent with upregulation of the mTOR pathway in human. Because a subset of radial glia were pS6 positive in the non-human primate samples, we hypothesized that primate radial glia have the capacity to further activate the mTOR pathway in the presence of upstream factors. We therefore treated primary macaque cells in monolayer and organotypic culture with BDNF and the MTOR activator 3-Benzyl-5-((2-nitrophenoxy)methyl)-dihydrofuran-2(3H)-one (3BDO) (Peng et al., 2014). Both activators led to increased pS6 levels in progenitors (Figure S6). This finding suggests that, across primates, cortical progenitors are responsive to the mTOR pathway, but that human radial glia show a higher level of activation (Figure S6). To further probe for candidate upstream regulators explaining the increased activation in human progenitors, we examined whether INSR and ITGB8, two receptors upregulated in human, were necessary for normal pS6 activation in organotypic slice culture of primary human samples. We infected slices with short hairpin RNA (shRNA) lentiviral vectors targeting each gene and found that reducing INSR and ITGB reduced overall levels of pS6 (Figure 6C). Together, these results provide a candidate molecular mechanism governing human-specific changes in cortical radial glia signaling pathways.

DISCUSSION

Over the last six million years, genetic changes along the human lineage have driven remarkable changes in human brain structure, cognition, and behavior. These genetic changes likely influenced patterns of brain development because brain size differences appear in utero, and nearly all cortical neurons are generated prior to birth (Sakai et al., 2012). Thus, comparative studies of brain development are essential for understanding the molecular basis of human brain evolution. Genetic changes are particularly likely to influence gene expression, either directly through copy number or cis-regulatory changes or indirectly through the trans-regulatory effects of genes harboring mutations. However, in contrast to adult samples, prenatal brain tissue from chimpanzee, our closest living relative, is largely inaccessible to analyses of gene expression. Here, we sought to establish great ape cerebral organoids as a model system for studying human-specific molecular changes that influence neurogenesis. We found that gene regulatory mechanisms observed during neurogenesis in primary cortex are mostly recapitulated in organoid models, and we identified human-specific gene expression patterns during cortical neurogenesis through independent comparisons of human and primate primary cells and organoid models.

Because cerebral organoids are a relatively new model system, we developed a multi-dimensional report card of the correspondence between human cerebral organoids and primary tissue. Our findings indicate that organoid cell composition can vary across experiments, individuals, and protocols, but that underlying cell types, gene co-expression relationships, and developmental trajectories are preserved in organoid models across individuals, species, and protocols. The pathways distinguishing organoids—glycolysis, endoplasmic reticulum stress, and electron transport—provide useful targets for further optimization of cerebral organoid media and perfusion conditions and may also have implications for organoid studies of neurodegenerative disorders in which cellular stress pathways are known to accelerate the appearance of disease phenotypes. Together, our report card reveals the fidelity and robustness of developmental programs that can be modeled using cerebral organoids, and serves as a data-driven framework for evaluating organoid cells along biological axes of variation related to cell heterogeneity, neuronal differentiation, radial glia maturation, cortical arealization, and metabolic states. From the report card analysis, we conclude that comparative investigation of organoid models across species provides a realistic window into gene regulatory changes in cortical evolution, but that independent analysis of primary cells from different species still provides crucial validation data independent from organoid models for determining species-specific gene expression patterns. Future improvements to organoid protocols that demonstrate reproducibility of cell composition and neuronal connectivity relationships may enable evolutionary analysis of addition facets of human and great ape brain development beyond this initial focus on gene regulation.

Human-specific genetic changes may affect cortical development by influencing gene regulatory networks active during neurogenesis. Although there is great interest in modeling the

impact of human-specific genetic changes on brain development (Boyd et al., 2015; McLean et al., 2011; Pollard et al., 2006; Charrier et al., 2012; Dennis et al., 2012; Florio et al., 2016), a description of actual molecular differences during normal development is crucial for interpreting the consequences of genome sequence changes. Against a background of highly conserved gene expression patterns, we identify 261 candidate genes with derived expression changes in the human lineage. A subset of these changes are concerted across non-neural cell types, but the majority appear to be specific to developing cortex and shared across cortical cell types. These results are consistent with a hierarchical model in which regulatory mutations have different levels of pleiotropy from organism to tissue to cell type (Liang et al., 2018). In addition to individual genes, we identified several gene co-expression modules with increased expression along the human lineage, including modules enriched for genes affecting transcription during the G1/S transition and neuronal apoptosis, two developmental processes that may influence the number of progenitors and neurons. Future analysis of hub genes and candidate upstream factors in these networks may illuminate the causative genetic changes underlying gene expression differences. In addition, the recent *de novo* assembly of the chimpanzee genome and improved gene models enabled more accurate measurements of gene expression as a result of higher alignment rates to the native genome of each species (Kronenberg et al., 2018; Fiddes et al., 2018). Nonetheless, the annotation of gene models and expression levels of some genes may still be biased toward the higher quality human genome assembly, in particular, with respect to macaque. Therefore, future improvements of gene annotations and genome assembly through long read sequencing in other primates will further strengthen comparative analyses. In addition, increased cellular coverage through droplet capture of single cells across many individuals and stages will make analysis more comprehensive, illuminating the most divergent gene networks, cell types, and developmental trajectories.

Several influential models suggest that human brain expansion may result from an increase in the number of radial glia early in development (Rakic, 2003), an increase in the number of outer subventricular zone progenitors (Fish et al., 2008; Kriegstein et al., 2006; Smart et al., 2002), and an extended neurogenic window (Rakic, 1995). In each of these models, signaling pathways controlling radial glia expansion and self-renewal represent candidate molecular pathways that could explain changes in developmental cell behavior. We recently observed increased activation of the LIFR-STAT3 self-renewal pathway in outer subventricular zone radial glia compared to ventricular radial glia that could support selective expansion of this secondary proliferative population during cortical development. However, this molecular signature was conserved in macaque radial glia and not likely related to more recent human brain evolution (Pollen et al., 2015). Here, our comparative transcriptomic data among primates allowed us to examine additional signaling pathways that may have changed in more recent evolution. We find evidence that an increase in the activity of another key signaling pathway, PI3K-AKT-mTOR, distinguishes human outer subventricular zone radial glia from those in other primates. In many stem cell contexts, the mTOR pathway has been shown to pro-

mote stemness and long-term self-renewal (Zhou et al., 2009; Rafalski and Brunet, 2011). While it is possible that the increased levels of mTOR activation could be a consequence of increased proliferation in human radial glia, our results indicate that radial glia across primates are poised to activate mTOR signaling and suggest that increased levels of INSR and ITGB8 in human may contribute to recent evolutionary changes in pathway activation. Importantly, mTOR pathway mutations are associated with several human disorders, including autism, focal cortical dysplasia, and glioblastoma multiforme (Poduri et al., 2012; Ceccarelli et al., 2016). Our results suggest that during development, human outer subventricular zone radial glia may be particularly sensitive to perturbations in this pathway, and future studies may more directly assess the role of this pathway in human and primate neurogenesis. Together with recent work, our study adds to a burgeoning field of "cellular anthropology" (Prescott et al., 2015) by providing a comparative organoid platform for systematically characterizing the specialized molecular features of human cortical development and evolution.

STAR★METHODS

Detailed methods are provided in the online version of this paper and include the following:

- KEY RESOURCES TABLE
- CONTACT FOR REAGENT AND RESOURCE SHARING
- EXPERIMENTAL MODEL AND SUBJECT DETAILS
  - Cell lines and Samples
  - Organoid Differentiation Protocol
- METHOD DETAILS
  - Immunohistochemistry
  - Single cell RNA sequencing
  - *In Situ* Hybridization
  - Primary Dissociated Samples
  - Primary Organotypic Slice Cultures
  - Alignments and gene models
  - De-multiplexing chimeric organoids
  - Clustering and Determining homologous cell types
  - Determining co-expression modules
  - Differential expression and enrichment analysis
  - Western blots
- QUANTIFICATION AND STATISTICAL ANALYSIS
- DATA AND SOFTWARE AVAILABILITY

AUTHOR CONTRIBUTIONS

DECLARATION OF INTERESTS

REFERENCES

Bakken, T.E., Miller, J.A., Ding, S.-L., Sunkin, S.M., Smith, K.A., Ng, L., Szafer, A., Dalley, R.A., Royall, J.J., Lemon, T., et al. (2016). A comprehensive transcriptional map of primate brain development. Nature 535, 367–375.

Bershteyn, M., Nowakowski, T.J., Pollen, A.A., Di Lullo, E., Nene, A., Wynshaw-Boris, A., and Kriegstein, A.R. (2017). Human iPSC-derived cerebral organoids model cellular features of lissencephaly and reveal prolonged mitosis of outer radial glia. Cell Stem Cell 20, 435–449.

Blake, L.E., Thomas, S.M., Blischak, J.D., Hsiao, C.J., Chavarria, C., Myrthil, M., Gilad, Y., and Pavlovic, B.J. (2018). A comparative study of endoderm differentiation in humans and chimpanzees. Genome Biol. 19, 162.

Boyd, J.L., Skove, S.L., Rouanet, J.P., Pilaz, L.-J., Bepler, T., Gordân, R., Wray, G.A., and Silver, D.L. (2015). Human-chimpanzee differences in a FZD8 enhancer alter cell-cycle dynamics in the developing neocortex. Curr. Biol. 25, 772–779.

Butler, A., Hoffman, P., Smibert, P., Papalexi, E., and Satija, R. (2018). Integrating single-cell transcriptomic data across different conditions, technologies, and species. Nat. Biotechnol. 36, 411–420.

Camp, J.G., Badsha, F., Florio, M., Kanton, S., Gerber, T., Wilsch-Bräuninger, M., Lewitus, E., Sykes, A., Hevers, W., Lancaster, M., et al. (2015). Human cerebral organoids recapitulate gene expression programs of fetal neocortex development. Proc. Natl. Acad. Sci. USA 112, 15672–15677.

Casper, J., Zweig, A.S., Villarreal, C., Tyner, C., Speir, M.L., Rosenbloom, K.R., Raney, B.J., Lee, C.M., Lee, B.T., Karolchik, D., et al. (2018). The UCSC Genome Browser database: 2018 update. Nucleic Acids Res. 46, D762–D769.

Ceccarelli, M., Barthel, F.P., Malta, T.M., Sabedot, T.S., Salama, S.R., Murray, B.A., Morozova, O., Newton, Y., Radenbaugh, A., Pagnotta, S.M., et al.; TCGA Research Network (2016). Molecular profiling reveals biologically discrete subsets and pathways of progression in diffuse glioma. Cell 164, 550–563.

Charrier, C., Joshi, K., Coutinho-Budd, J., Kim, J.-E., Lambert, N., de Marchena, J., Jin, W.-L., Vanderhaeghen, P., Ghosh, A., Sassa, T., and Polleux, F. (2012). Inhibition of SRGAP2 function by its human-specific paralogs induces neoteny during spine maturation. Cell 149, 923–935.

Chen, E.Y., Tan, C.M., Kou, Y., Duan, Q., Wang, Z., Meirelles, G.V., Clark, N.R., and Ma'ayan, A. (2013). Enrichr: Interactive and collaborative HTML5 gene list enrichment analysis tool. BMC Bioinformatics 14, 128.

Clevers, H. (2016). Modeling development and disease with organoids. Cell 165, 1586–1597.

Dennis, M.Y., Nuttle, X., Sudmant, P.H., Antonacci, F., Graves, T.A., Nefedov, M., Rosenfeld, J.A., Sajjadian, S., Malig, M., Kotkiewicz, H., et al. (2012). Evolution of human-specific neural SRGAP2 genes by incomplete segmental duplication. Cell 149, 912–922.

Dennis, M.Y., Harshman, L., Nelson, B.J., Penn, O., Cantsilieris, S., Huddleston, J., Antonacci, F., Penewit, K., Denman, L., Raja, A., et al. (2017). The evolution and population diversity of human-specific segmental duplications. Nat. Ecol. Evol. 1, 69.

Eiraku, M., Watanabe, K., Matsuo-Takasaki, M., Kawada, M., Yonemura, S., Matsumura, M., Wataya, T., Nishiyama, A., Muguruma, K., and Sasai, Y. (2008). Self-organized formation of polarized cortical tissues from ESCs and its active manipulation by extrinsic signals. Cell Stem Cell 3, 519–532.

Eiraku, M., Takata, N., Ishibashi, H., Kawada, M., Sakakura, E., Okuda, S., Sekiguchi, K., Adachi, T., and Sasai, Y. (2011). Self-organizing optic-cup morphogenesis in three-dimensional culture. Nature 472, 51–56.

Fiddes, I.T., Armstrong, J., Diekhans, M., Nachtweide, S., Kronenberg, Z.N., Underwood, J.G., Gordon, D., Earl, D., Keane, T., Eichler, E.E., et al. (2018). Comparative Annotation Toolkit (CAT)-simultaneous clade and personal genome annotation. Genome Res. 28, 1029–1038.

Fish, J.L., Dehay, C., Kennedy, H., and Huttner, W.B. (2008). Making bigger brains-the evolution of neural-progenitor-cell division. J. Cell Sci. 121, 2783–2793.

Florio, M., Namba, T., Pääbo, S., Hiller, M., and Huttner, W.B. (2016). A single splice site mutation in human-specific ARHGAP11B causes basal progenitor amplification. Sci. Adv. 2, e1601941.

Gallego Romero, I., Pavlovic, B.J., Hernando-Herraez, I., Zhou, X., Ward, M.C., Banovich, N.E., Kagan, C.L., Burnett, J.E., Huang, C.H., Mitrano, A., et al. (2015). A panel of induced pluripotent stem cells from chimpanzees: A resource for comparative functional genomics. eLife 4, e07103.

Herculano-Houzel, S. (2012). The remarkable, yet not extraordinary, human brain as a scaled-up primate brain and its associated cost. Proc. Natl. Acad. Sci. USA 109 (Suppl 1), 10661–10668.

Hoffman, G.E., and Schadt, E.E. (2016). variancePartition: Interpreting drivers of variation in complex gene expression studies. BMC Bioinformatics 17, 483.

Johnson, M.E., Viggiano, L., Bailey, J.A., Abdul-Rauf, M., Goodwin, G., Rocchi, M., and Eichler, E.E. (2001). Positive selection of a gene family during the emergence of humans and African apes. Nature 413, 514–519.

Kadoshima, T., Sakaguchi, H., Nakano, T., Soen, M., Ando, S., Eiraku, M., and Sasai, Y. (2013). Self-organization of axial polarity, inside-out layer pattern, and species-specific progenitor dynamics in human ES cell-derived neocortex. Proc. Natl. Acad. Sci. USA 110, 20284–20289.

Kent, W.J., Baertsch, R., Hinrichs, A., Miller, W., and Haussler, D. (2003). Evolution's cauldron: duplication, deletion, and rearrangement in the mouse and human genomes. Proc. Natl. Acad. Sci. USA 100, 11484–11489.

Kreitzer, F.R., Salomonis, N., Sheehan, A., Huang, M., Park, J.S., Spindler, M.J., Lizarraga, P., Weiss, W.A., So, P.L., and Conklin, B.R. (2013). A robust method to derive functional neural crest cells from human pluripotent stem cells. Am. J. Stem Cells 2, 119–131.

Kriegstein, A., Noctor, S., and Martínez-Cerdeño, V. (2006). Patterns of neural stem and progenitor cell division may underlie evolutionary cortical expansion. Nat. Rev. Neurosci. 7, 883–890.

Kronenberg, Z.N., Fiddes, I.T., Gordon, D., Murali, S., Cantsilieris, S., Meyerson, O.S., Underwood, J.G., Nelson, B.J., Chaisson, M.J.P., Dougherty, M.L., et al. (2018). High-resolution comparative analysis of great ape genomes. Science 360, eaar6343.

Lancaster, M.A., Renner, M., Martin, C.-A., Wenzel, D., Bicknell, L.S., Hurles, M.E., Homfray, T., Penninger, J.M., Jackson, A.P., and Knoblich, J.A. (2013). Cerebral organoids model human brain development and microcephaly. Nature 501, 373–379.

Langfelder, P., and Horvath, S. (2008). WGCNA: An R package for weighted correlation network analysis. BMC Bioinformatics 9, 559.

Lefebvre, V. (2008). Fast unfolding of communities in large networks. J. Stat. Mech. *2008*, P10008.

Liang, C., Musser, J.M., Cloutier, A., Prum, R.O., and Wagner, G.P. (2018). Pervasive Correlated Evolution in Gene Expression Shapes Cell and Tissue Type Transcriptomes. Genome Biol. Evol. *10*, 583–552.

Marchetto, M.C.N., Narvaiza, I., Denli, A.M., Benner, C., Lazzarini, T.A., Nathanson, J.L., Paquola, A.C.M., Desai, K.N., Herai, R.H., Weitzman, M.D., et al. (2013). Differential L1 regulation in pluripotent stem cells of humans and apes. Nature *503*, 525–529.

Matsumoto, Y., Hayashi, Y., Schlieve, C.R., Ikeya, M., Kim, H., Nguyen, T.D., Sami, S., Baba, S., Barruet, E., Nasu, A., et al. (2013). Induced pluripotent stem cells from patients with human fibrodysplasia ossificans progressive show increased mineralization and cartilage formation. Orphanet. J. Rare Dis. *8*, 190.

McLean, C.Y., Reno, P.L., Pollen, A.A., Bassan, A.I., Capellini, T.D., Guenther, C., Indjeian, V.B., Lim, X., Menke, D.B., Schaar, B.T., et al. (2011). Human-specific loss of regulatory DNA and the evolution of human-specific traits. Nature *471*, 216–219.

Mora-Bermúdez, F., Badsha, F., Kanton, S., Camp, J.G., Vernot, B., Köhler, K., Voigt, B., Okita, K., Maricic, T., He, Z., et al. (2016). Differences and similarities between human and chimpanzee neural progenitors during cerebral cortex development. eLife *5*, 166.

Noctor, S.C., Flint, A.C., Weissman, T.A., Dammerman, R.S., and Kriegstein, A.R. (2001). Neurons derived from radial glial cells establish radial units in neocortex. Nature *409*, 714–720.

Nowakowski, T.J., Bhaduri, A., Pollen, A.A., Alvarado, B., Mostajo-Radji, M.A., Di Lullo, E., Haeussler, M., Sandoval-Espinosa, C., Liu, S.J., Velmeshev, D., et al. (2017). Spatiotemporal gene expression trajectories reveal developmental hierarchies of the human cortex. Science *358*, 1318–1323.

Ohno, S. (1970). Evolution by Gene Duplication (Springer Berlin Heidelberg).

Okita, K., Matsumura, Y., Sato, Y., Okada, A., Morizane, A., Okamoto, S., Hong, H., Nakagawa, M., Tanabe, K., Tezuka, K., et al. (2011). A more efficient method to generate integration-free human iPSC cells. Nat. Methods *8*, 409–412.

Oldham, M.C., Konopka, G., Iwamoto, K., Langfelder, P., Kato, T., Horvath, S., and Geschwind, D.H. (2008). Functional organization of the transcriptome in human brain. Nat. Neurosci. *11*, 1271–1282.

Onorati, M., Li, Z., Liu, F., Sousa, A.M.M., Nakagawa, N., Li, M., Dell'Anno, M.T., Gulden, F.O., Pochareddy, S., Tebbenkamp, A.T.N., et al. (2016). Zika virus disrupts phospho-tbk1 localization and mitosis in human neuroepithelial stem cells and radial glia. Cell Rep. *16*, 2576–2592.

Otani, T., Marchetto, M.C., Gage, F.H., Simons, B.D., and Livesey, F.J. (2016). 2D and 3D stem cell models of primate cortical development identify species-specific differences in progenitor behavior contributing to brain size. Cell Stem Cell *18*, 467–480.

Paten, B., Earl, D., Nguyen, N., Diekhans, M., Zerbino, D., and Haussler, D. (2011). Cactus: Algorithms for genome multiple sequence alignment. Genome Res. *21*, 1512–1528.

Pavlovic, B.J., Blake, L.E., Roux, J., Chavarria, C., and Gilad, Y. (2018). A comparative assessment of human and chimpanzee iPSC-derived cardiomyocytes with primary heart tissues. Sci. Rep. *8*, 15312.

Peng, N., Meng, N., Wang, S., Zhao, F., Zhao, J., Su, L., Zhang, S., Zhang, Y., Zhao, B., and Miao, J. (2014). An activator of mTOR inhibits oxLDL-induced autophagy and apoptosis in vascular endothelial cells and restricts atherosclerosis in apolipoprotein E$^{-/-}$ mice. Sci. Rep. *4*, 5519.

Poduri, A., Evrony, G.D., Cai, X., Elhosary, P.C., Beroukhim, R., Lehtinen, M.K., Hills, L.B., Heinzen, E.L., Hill, A., Hill, R.S., et al. (2012). Somatic activation of AKT3 causes hemispheric developmental brain malformations. Neuron *74*, 41–48.

Pollard, K.S., Salama, S.R., Lambert, N., Lambot, M.-A., Coppens, S., Pedersen, J.S., Katzman, S., King, B., Onodera, C., Siepel, A., et al. (2006). An RNA gene expressed during cortical development evolved rapidly in humans. Nature *443*, 167–172.

Pollen, A.A., Nowakowski, T.J., Shuga, J., Wang, X., Leyrat, A.A., Lui, J.H., Li, N., Szpankowski, L., Fowler, B., Chen, P., et al. (2014). Low-coverage single-cell mRNA sequencing reveals cellular heterogeneity and activated signaling pathways in developing cerebral cortex. Nat. Biotechnol. *32*, 1053–1058.

Pollen, A.A., Nowakowski, T.J., Chen, J., Retallack, H., Sandoval-Espinosa, C., Nicholas, C.R., Shuga, J., Liu, S.J., Oldham, M.C., Diaz, A., et al. (2015). Molecular identity of human outer radial glia during cortical development. Cell *163*, 55–67.

Prescott, S.L., Srinivasan, R., Marchetto, M.C., Grishina, I., Narvaiza, I., Selleri, L., Gage, F.H., Swigut, T., and Wysocka, J. (2015). Enhancer divergence and cis-regulatory evolution in the human and chimp neural crest. Cell *163*, 68–83.

Quadrato, G., Nguyen, T., Macosko, E.Z., Sherwood, J.L., Min Yang, S., Berger, D.R., Maria, N., Scholvin, J., Goldman, M., Kinney, J.P., et al. (2017). Cell diversity and network dynamics in photosensitive human brain organoids. Nature *545*, 48–53.

Rafalski, V.A., and Brunet, A. (2011). Energy metabolism in adult neural stem cell fate. Prog. Neurobiol. *93*, 182–203.

Rakic, P. (1995). A small step for the cell, a giant leap for mankind: A hypothesis of neocortical expansion during evolution. Trends Neurosci. *18*, 383–388.

Rakic, P. (2003). Developmental and evolutionary adaptations of cortical radial glia. Cereb. Cortex *13*, 541–549.

Sakai, T., Hirata, S., Fuwa, K., Sugama, K., Kusunoki, K., Makishima, H., Eguchi, T., Yamada, S., Ogihara, N., and Takeshita, H. (2012). Fetal brain development in chimpanzees versus humans. Curr. Biol. *22*, R791–R792.

Shekhar, K., Lapan, S.W., Whitney, I.E., Tran, N.M., Macosko, E.Z., Kowalczyk, M., Adiconis, X., Levin, J.Z., Nemesh, J., Goldman, M., et al. (2016). Comprehensive classification of retinal bipolar neurons by single-cell transcriptomics. Cell *166*, 1308–1323.

Sherry, S.T., Ward, M.H., Kholodov, M., Baker, J., Phan, L., Smigielski, E.M., and ad Sirotkin, K. (2001). dbSNP: the NCBI database of genetic variation. Nucleic Acids Res. *29*, 308–311.

Silver, D.L. (2016). Genomic divergence and brain evolution: How regulatory DNA influences development of the cerebral cortex. BioEssays *38*, 162–171.

Sloan, S.A., Darmanis, S., Huber, N., Khan, T.A., Birey, F., Caneda, C., Reimer, R., Quake, S.R., Barres, B.A., and Paşca, S.P. (2017). Human astrocyte maturation captured in 3D cerebral cortical spheroids derived from pluripotent stem cells. Neuron *95*, 779–790.

Smart, I.H.M.I., Dehay, C., Giroud, P., Berland, M., and Kennedy, H. (2002). Unique morphological features of the proliferative zones and postmitotic compartments of the neural epithelium giving rise to striate and extrastriate cortex in the monkey. Cereb. Cortex *12*, 37–53.

Stessman, H.A.F., Xiong, B., Coe, B.P., Wang, T., Hoekzema, K., Fenckova, M., Kvarnung, M., Gerdts, J., Trinh, S., Cosemans, N., et al. (2017). Targeted sequencing identifies 91 neurodevelopmental-disorder risk genes with autism and developmental-disability biases. Nat. Genet. *49*, 515–526.

Sudmant, P.H., Kitzman, J.O., Antonacci, F., Alkan, C., Malig, M., Tsalenko, A., Sampas, N., Bruhn, L., Shendure, J., and Eichler, E.E.; 1000 Genomes Project (2010). Diversity of human copy number variation and multicopy genes. Science *330*, 641–646.

Sudmant, P.H., Huddleston, J., Catacchio, C.R., Malig, M., Hillier, L.W., Baker, C., Mohajeri, K., Kondova, I., Bontrop, R.E., Persengiev, S., et al.; Great Ape Genome Project (2013). Evolution and diversity of copy number variation in the great ape lineage. Genome Res. *23*, 1373–1382.

Zhou, J., Su, P., Wang, L., Chen, J., Zimmermann, M., Genbacev, O., Afonja, O., Horne, M.C., Tanaka, T., Duan, E., et al. (2009). mTOR supports long-term self-renewal and suppresses mesoderm and endoderm activities of human embryonic stem cells. Proc. Natl. Acad. Sci. USA *106*, 7840–7845.

STAR★METHODS

KEY RESOURCES TABLE

REAGENT or RESOURCE	SOURCE	IDENTIFIER
Antibodies		
anti-TBR2, sheep, 1:150	R&D Systems	Cat# AF6166; RRID: AB_10569705
anti-pS6, rabbit, 1:100	Cell Signaling	Cat# 2211S; RRID: AB_331679
anti-SOX2, goat, 1:200	Santa Cruz Biotechnology	Cat# SC17320; RRID: AB_2286684
anti-SOX2, mouse, 1:200	Santa Cruz Biotechnology	Cat# SC365964
anti-TUJ1, mouse, 1:500	Covance	Cat# MMS-435; RRID: AB_2313773
anti-PAX6, rabbit, 1:500	Covance	Cat# PRB-278P; RRID: AB_291612
anti-CTIP2, rat, 1:500	Abcam	Cat# ab18465; RRID: AB_2064130
anti-TBR1, rabbit, 1:500	Abcam	Cat# ab31940; RRID: AB_2200219
anti-SATB2, rabbit, 1:1000	Abcam	Cat# ab34735; RRID: AB_2301417
anti-GFP, goat, 1:500	Abcam	Cat# ab5450; RRID: AB_304897
anti-pNRDG1, rabbit, 1:1000	Cell Signaling	Cat# 5482; RRID: AB_10693451
anti-p4EBP1, rabbit, 1:1000	Cell Signaling	Cat# 2855; RRID: AB_560835
anti-INSR, rabbit, 1:1000	Novus Biologicals	Cat# NBP2-12793
anti-β-tubulin, mouse, 1:1000	Millipore Sigma	Cat# A1978; RRID: AB_476692
Bacterial and Virus Strains		
CMV::GFP adenovirus	Vector Biolabs	Cat# 1060
Chemicals, Peptides, and Recombinant Proteins		
Rapamycin, 250 nM	Abcam	Cat# ab146591
BDNF, 20ng/mL	Millipore Sigma	Cat# SRP3014-10
3-Benzyl-5-((2-nitrophenoxy)methyl)-dihydrofuran-2(3H)-one (3BDO) (Peng et al., 2014), 60uM	Millipore Sigma	Cat# SML1687
Rock Inhibitor Y-27632	Tocris	Cat# 1254
IWR-1-endo	Cayman Chemical	Cat# 13659
SB431542	Tocris	Cat# 1614
Deposited Data		
Raw and processed organoid and macaque data	This paper	GEO: GSE124299
Raw and processed primary human data	Nowakowski et al., 2017	dbGaP: phs000989.v3
Experimental Models: Cell Lines		
C1-PR00738-male	This paper	RRID: CVCL_2X19
C2-S003649-male	Gilad lab; Gallego Romero et al., 2015	RRID: CVCL_1G31
C3-S008861-male	Gilad lab; Gallego Romero et al., 2015	RRID: CVCL_1G34
C4-40290G-male	Gilad lab; Pavlovic et al., 2018	
C5-S004955-male	Gilad lab; Gallego Romero et al., 2015	RRID: CVCL_1G33
C6-40210A-male	Gilad lab; Gallego Romero et al., 2015	RRID: CVCL_1G35
C7A-S003611-male	This paper	RRID: CVCL_V833
C7B-S003611-male	This paper	RRID: CVCL_V833
C8-PR00226-male	This paper	RRID: CVCL_2V65
H1-CRL-2522-male	Hsiao lab; Matsumoto et al., 2013	RRID: CVCL_3653

(Continued on next page)

Continued

REAGENT or RESOURCE	SOURCE	IDENTIFIER
H2A-1323.2-female	Hsiao lab; Matsumoto et al., 2013	RRID: CVCL_0G83
H2B-1323.4-female	Hsiao lab; Matsumoto et al., 2013	RRID: CVCL_0G84
H3-GM25256-male	Conklin lab; Kreitzer et al., 2013	RRID: CVCL_Y803
H4-IPSC.C-male	Bucay lab	N/A
H5-28815-male	Gilad-26102527	N/A
H6-28126-male	Gilad-26102527	N/A
H7-CESCG-295-male	Wang lab-CESCG	N/A
H8-H23555A-male	Gilad-26102527	N/A
H9-SSC-PB1-male	Wang lab –CESCG	N/A
H10-CESCG-297-male	Wang lab –CESCG	N/A
Oligonucleotides		
SRCAP *in situ* probe sequence: ATTTAGGTGACACTATAGCCGCCTACCCCAAGAGGAGGAGGAGGGGGCCAGGGGCTGGGGATGAGAGTTCCTGTGGGACTGGTGGAGGCACCCACCGGCGCAGTAAAAAGGCCAAGGCCCCTGAGAGGCCAGGGACTCGTGTCAGTGAGCGTCTTCGTGGAGCCCGGGCTGAGACTCAAGGGGCAAACCACACTCCTGTCATATCCGCCCATCAAACTCGCAGCACCACCACACCGCCCCGCTGCAGTCCTGCCAGGGAGAGAGTTTCCAGGCCAGCACCTAGGCCTCGACCCACTCCAGCTTCAGCTCCAGCTGCAATTCCTGCCCTTGTTCCTGTCCCAGTCTCTGCCCCCAGTACCCATTTCAACCCCAAATCCAATAACCATTCTCCCTGTCCATATATTGCCTTCTCCCCCCCCCTCCACAGATTCCTCCTTGTTCTCCTGCCTGCACCCCTCCTCCCGCCTGTACCCTATAGTGAGTCGTATTACTC	IDT, this paper	N/A
SLC29A4 *in situ* probe sequence: ATTTAGGTGACACTATAGTGGCAGCTCTGCCCGTGGACTGGCGGGGCACCCACCTGCTGGCCTGCTCCTGCCTGCGCATAGTCTTCATCCCTCTCTTCATCCTGTGCGTCTACCCCAGCGGCACGCCCGCCCTGCGCCACCCCGCCTGGCCCTGCATCTTCTCGCTGCTTATGGGCATCAGCAACGGCTACTTCGGCAGCGTGCCCATGATCCTGGCGGCGGGCAAAGTGAGCCCCAAGCAGCGGGAGCTGGCAGGGAACACCATGACCGTGTCCTACATGTCGGGGCTGACACTGGGGTCCGCCGTGGCCTACTGCACCTACAGCCTCACCCGCGACGCCCACGGCAGCTGCCTGCACCCCTCCACCGCCAATGGCTCCATCCTCTCAGGCCTCTGAGCCAGCTCTGCCCACTGCCAGGGATGCCGAGGGCCTGACCAGGGGCCCCAAGGCCTGAAGGCCCCTCCCCCGTCCCCACCCTATAGTGAGTCGTATTACTC	IDT, this paper	N/A
Recombinant DNA		
pCXLE-hOCT3/4-shp53-F (OCT3/4 and p53 shRNA)	Okita et al., 2011	Addgene 27077
pCXLE-hSK (SOX2, KLF4)	Okita et al., 2011	Addgene 27078
pCXLE-hUL (L-MYC, LIN28)	Okita et al., 2011	Addgene 27080
pCXLE-EGFP (negative control)	Okita et al., 2011	Addgene 27082

CONTACT FOR REAGENT AND RESOURCE SHARING

Further information and requests for resources and reagents should be directed to and will be fulfilled by the Lead Contact, Alex A Pollen (Alex.Pollen@ucsf.edu).

EXPERIMENTAL MODEL AND SUBJECT DETAILS

Cell lines and Samples

We used previously described human and chimpanzee iPSC lines (Bershteyn et al., 2017; Gallego Romero et al., 2015; Pavlovic et al., 2018), and generated four additional lines from three chimpanzees (Table S1). All new lines were reprogrammed from fibroblasts using episomal plasmids according to a recently published protocol (Okita et al., 2011) and matching the protocol used for the

majority of existing human and chimpanzee lines used in this study (Table S1). Low passage fibroblasts (P3 – P7) were obtained from the Coriell Cell Repository (Pt1: 12 year old chimpanzee male, catalog: PR00226; Pt2: 6 year old chimpanzee male, Maverick, catalog: S003611; Pt5: 8 year old chimpanzee male, catalog PR00738). For each line, we electroporated 300,000 fibroblasts with three micrograms of an episomal expression plasmid mixture encoding OCT3/4, SOX2, KLF4, L-MYC, LIN28, and shRNA for TP53 using a Neon Electroporator (Thermo Fisher), and a 100 μL kit, with setting of 1,650V, 10ms, and three pulses, as previously described (Bershteyn et al., 2017). After 5 – 8 days, electroporated cells were detached and seeded onto irradiated SNL feeder cells. Culture medium was replaced the next day with primate ESC medium (Reprocell) containing 5 – 20 ng/mL of βFGF, with higher levels of FGF producing better results. After 20 – 30 days, colonies were picked and selected for further cultivation. After three to five passages, colonies were transferred to Matrigel-coated dishes and maintained in mTeSR1 medium (Stem Cell Technologies, 05850) supplemented with Penicillin/Streptomycin/Gentomycin. Further passaging was performed using calcium and magnesium free PBS to gently disrupt colonies. Each line showed a normal karyotype between passage 10 and 15. Macaque cortical tissue was generously provided from samples being used for other experiments from the UC Davis Primate Center. De-identified tissue samples were collected with previous patient consent in strict observance of the legal and institutional ethical regulations. Protocols, cell lines and samples were approved by UCSF GESCR (Gamete, Embryo, and Stem Cell Research) Committee.

Organoid Differentiation Protocol

We generated cerebral organoids according to previously published protocols (Kadoshima et al., 2013); (Bershteyn et al., 2017). Human and chimpanzee iPSCs were dissociated to single cells with Accutase and re-aggregated in lipidure-coated 96-well V-bottom plates at a density of 10,000 cells per aggregate, in 100 μL of cortical differentiation medium per well. The cortical differentiation medium (Glasgow-MEM, 20% KSR, 0.1mM NEAA, 1mM sodium pyruvate, 0.1mM β-ME, 100 U/mL penicillin/streptomycin) was supplemented with Rho Kinase Inhibitor (Y-27632, 20 μM, Tocris, Cat# 1254 day 0 and day 3), WNT inhibitor (IWR1-ε, 3 μM, Cayman Chemical Cat# 13659 days 0-18) and TGF-β inhibitor (SB431542, Tocris, Cat #1614, 5 μM, days 0-18). Media was changed on days 3 and 6 and then every 2-3 days until day 18. Aggregates were then transferred to ultra low adhesion 6-well plates in DMEM/F12 medium with Glutamax supplemented with N2, Lipid Concentrate, Fungizone (2.5 μg/mL), and penicillin/streptomycin (100 U/mL) and grown under 40% O2 5% CO2 conditions. After five weeks, FBS (10% v/v), Matrigel (1% v/v) and heparin (5 μg/mL) were added to the medium, and after 8 weeks organoids were transferred to lumox dishes (Sarstedt), which have a gas permeable base.

METHOD DETAILS

Immunohistochemistry

Organoids were fixed using 4% paraformaldehyde (PFA) in PBS for 20 min. Primary samples were fixed in 4% PFA prepared in calcium and magnesium free phosphate buffered saline (PBS) (pH~10) overnight at 4°C with constant agitation. After fixation, organoids and primary tissue samples were washed in PBS (pH7.4), equilibrated in 30% sucrose in PBS overnight at 4°C, embedded in blocks with a 1:1 mixture of 30% sucrose/OCT compound (Tissue-Tek, VWR) and frozen at −80°C. Blocks were sectioned to a thickness of 16-20 μm cryosections, and antigen retrieval was performed, by heating sections to 95° in 10mM sodium citrate (pH = 6.0) for 15 min. Sections were then permeabilized and blocked with 10% donkey serum in PBS in 2% Triton X-100, 0.2% gelatin. Primary antibody incubations were performed at 4°C overnight and secondary incubations were performed at room temperature for 1-3 hr, followed by three 20 min washes in PBS, and staining with AlexaFluor secondary antibodies (Thermo Fisher, 1:1000 dilution). Primary antibodies included: sheep anti-TBR2 (EOMES, 1:150, R&D AF6166), rabbit anti-pS6 (1:100, Cell Signaling 2211S), goat anti-SOX2 (1:200, Santa Cruz SC17320), mouse anti-SOX2 (1:200, Santa Cruz SC365964), Mouse anti-TUJ1 (β III TUBULIN, Covance, MMS-435, 1:500), rabbit anti-PAX6 (Covance, PRB-278P, 1:500), rat anti-CTIP2 (BCL11B, 1:500, Abcam ab18465), rabbit anti-TBR1 (1:500, Abcam ab31940), rabbit anti-SATB2 (1:1000, Abcam ab34735).

Single cell RNA sequencing

For single cell dissociation, primary and organoid samples were cut into small pieces, and incubated with a pre-warmed solution of Papain (Worthington Biochemical Corporation) prepared according to manufacturer's instructions for 10 min at 37°C. After approximately 30 – 60 min incubation, samples were triturated and macaque samples older than E100 and organoids older than 14 weeks were spun through an ovomucoid gradient to remove debris. Cells were then pelleted at 300 g and resuspended in PBS supplemented with 3% fetal bovine serum (Millipore Sigma). Samples were diluted to approximately 170,000 cells per ml before processing capture using Fluidigm C1 auto-prep system as previously described (Nowakowski et al., 2017; Pollen et al., 2014; 2015). We performed library preparation using the Illumina Nextera XT library preparation kit, and quantification using the Bioanalyzer (Agilent) according to manufacturer's protocols. Paired-end 100 bp sequencing was performed on the Illumina HiSeq2500.

In Situ Hybridization

Macaque (E64, 67, 80) and human (GW 13, 17, 19) tissue was fixed in 4% PFA in PBS overnight at 4°C with constant agitation and then embedded in a 50% O.C.T. (Sakura Finetek, 4583), 30% sucrose mix and frozen at −80°C. Tissue was cryosectioned at 16um thickness onto glass slides, post-fixed and hybridized for one hour at 70°C. Hybridization buffer contains 50% formamide, 5X SSC

buffer, 5X Denhart's solution (Thermo Fisher, 750018), 500ug/ml fish sperm DNA (Sigma, 11467140001) and 250ug/ml yeast RNA (Sigma, 10109223001). Hybridized tissue was incubated overnight at 70°C with riboprobes designed against a conserved region of the macaque and human transcripts for each gene of interest (See Key Resources Table). Probes were made using a T7 Mega-script kit (Invitrogen, AM1334) with DIG RNA labeling mix (Roche, 11277073910). Tissue was washed and incubated with an anti-DIG antibody (Roche, 1109327491) for 80 minutes at room temperature. Sections were developed using a NBT/BCIP (Roche, 11681451001) solution for 12-72 hours until a sufficient intensity. Slides treated with the same probe were incubated for the same duration of time. Slides were stopped by three PBS washes, coverslipped using Prolong Gold (Thermo Fisher P36930) and dried overnight. Tissue sections were imaged using a Keyence BZ-X fluorescent microscope.

Primary Dissociated Samples

Culture dishes were prepared by overnight coating with 0.01% poly-L-ornithine (Millipore Sigma) at 37°C. After three water washes, plates were coated with 5 ug/ml laminin (Thermo Fisher) and 1 ug/ml fibronectin (Corning) for at least two hours. Following dissociation, cells were cultured as previously reported (Onorati et al., 2016). Unless otherwise indicated, the media contained N2 Supplement (1:100, GIBCO), B27 supplement (1:1000, Thermo Fisher), FGF-2 (20 ng/ml, GIBCO), EGF (20 ng/ml, GIBCO), Human Insulin (20 ug/ml, Santa Cruz Biotechnology), BDNF (5 ng/ml, R&D Systems Inc), Rock Inhibitor Y-27632 (10 uM, Stemgent), Penicillin/Streptomycin (100 U/ml) in DMEM/F12+GlutamaxTM-I (GIBCO). Media was replaced every 3 days and cells were passaged were passaged when cultures reached ∼80% confluency (approximately every 5-7 days).

For mTOR experiments, cultures were depleted of BDNF from culture media for four days prior to being treated with either DMSO (1:500), 250nM Rapamycin (Abcam, ab146591), 20ng/mL BDNF (Millipore Sigma, srp3014-10) or 6uM 3BDO (Millipore Sigma, SML1687) for five days. A cmv::gfp adenovirus (1: 2,000, Vector biolabs, 1060) was added to the culture 24 hours prior to collection to detect morphological changes. Dissociated cells were fixed in the culture dish with 4% PFA in PBS for 45mins at 4°C. Cells were permeabilized and blocked with 10% donkey serum in PBS in 0.1% Triton X-100, 0.2% gelatin for 30 minutes. Primary antibodies were incubated at 4°C overnight, washed three times with PBS containing 0.1% Triton for 5 minutes and secondary antibodies incubated at room temperature for two hours. Antibodies included: goat anti-gfp (1:500, Abcam Ab5450), rabbit anti-pS6 (1:500, Cell Signaling 2211S) and mouse anti-SOX2 (1:200, Santa Cruz SC365964) and AlexaFluor secondary antibodies (Invitrogen, 1:1000 dilution). Dissociated cultures were imaged using a Keyence BZ-X fluorescent microscope.

Primary Organotypic Slice Cultures

Primary human (GW17-18) and macaque (E80) tissue was live sectioned with a vibratome at a thickness of 300uM. Slices were infected with cmv::gfp adenovirus (1: 2,000, Vector biolabs, 1060) for 30 minutes at 37°C and then plated on Millicell inserts (Millipore, PICM03050) in media containing 60% Basal Medium Eagle (BME) (Thermo Fisher 21010046), 25% Hank's BSS (UCSF cell culture facility CCFAJ001-171602), 10% FBS (Thermo Fisher, 16000044), 1% penicillin, streptomycin and glutamine (Thermo Fisher 10378016), 1% N-2 (Thermo Fisher, 17502048), and 0.66% d-(+)-glucose. One day after collection slices were infected with shRNA-containing lentivirus (Sigma TRCN0000000381 [shINSR] and Sigma TRCN0000413303 [shITGB8]) for 24 hours. After virus removal, the slices were cultured for an additional 4 days. Slices were fixed in 4% PFA in PBS for 1 hour at room temperature and washed with PBS overnight at 4°C. Antigen retrieval was performed on slices using 10x Citrate Buffer (Sigma, C9999) by incubating slices in solution heated to 90°C for 20 minutes. Slices were washed with PBS prior to being permeabilized and blocked with 10% donkey serum in PBS containing 0.1% Triton X-100 and 0.2% gelatin for 30 minutes. Slices were incubated with primary antibodies for 48 hours at 4°C, then washed three times with PBS with 0.1% Triton for a total of three hours. Slices were incubated in secondary antibodies at 4°C overnight. Primary antibodies used were goat anti-gfp (1:500, Abcam Ab5450), rabbit anti-pS6 (1:500, Cell Signaling 2211S), mouse anti-SOX2 (1:250, Santa Cruz SC365964) and rat anti-CTIP2 (BCL11B, 1:500, Abcam ab18465) and AlexaFluor secondary antibodies (Invitrogen, 1:500 dilution). Slices were imaged using a Leica sp5 X confocal microscope, and quantification was performed on pS6-labeled cells and DAPI labeled cells, as DAPI showed the most consistent labeling across slices.

Alignments and gene models

Trim Galore 3.7 was used to trim 20 bp of adaptor sequence, and paired-end alignments were performed using HISAT2 to the human reference genome GRCh38, the updated chimpanzee reference genome panTro6 (Kronenberg et al., 2018) or the macaque reference genome, rheMac8. For each cell, counts were determined using the subread-1.5.0 function featureCounts, and counts were normalized to counts per million. To determine orthologous genes across species, whole genome alignments between GRCh38 and either the current primate references (panTro4, gorGor4, ponAbe2, rheMac8) or the updated great ape references panTro6 (Kronenberg et al., 2018) were generated using progressiveCactus (Paten et al., 2011). Outgroup genomes were gibbon (nomLeu3), bushbaby (otoGar3), squirrel monkey (saiBol1) and mouse (mm10). These alignments were then used as input to CAT, using the GENCODE V27 annotation of GRCh38 as the annotation input. Species-specific RNA-seq and IsoSeq were used to help guide the annotation process (Fiddes et al., 2018). For this study, the resulting annotations on rheMac8 and the updated chimpanzee (panTro6) were used. CAT automatically defines orthology relationships using the information inherent in the whole genome alignment as well as subsequent filtering. This allows for quantification to be performed on the native species genome for a given

experiment, and the resulting gene counts can be compared across species by their unique gene identifiers. In total, 49,360 genes annotated in human were identified in both chimpanzee and rhesus.

De-multiplexing chimeric organoids

To identify the species of origin for each cell from RNA-seq data, we compiled a list of diagnostic loci where the chimpanzee and human genome assemblies differ by a single-base substitution mutation that shows no sign of being polymorphic. We then analyze the RNA-seq reads from each cell at these genomic loci and calculate the number of times that we observe the human or chimp base. We created the diagnostic SNPs by examining whole-genome alignments of human (hg19) against chimpanzee (panTro4), gorilla (gorGor3), orangutan (ponAbe2), and rhesus (rheMac3) (Casper et al., 2018). To conservatively filter for syntenic alignments, we removed alignments involving segments that have not been placed on chromosomes or that represent alternative haplotypes as well as mandating similarity scores of at least 10000 (Kent et al., 2003). With the remaining set of high quality alignments, we located positions in the human genome where chimpanzee had a different base from human and there was no current data to suggest the position was polymorphic in dbSnp (Sherry et al., 2001). To guard against highly variable sites or alignment ambiguity, we ensured that at least one outgroup species (gorilla, orangutan, and rhesus) was present and the outgroup species agreed with either chimpanzee or human. This resulted in approximately 15 million diagnostic positions. For each single-cell RNA-seq library we mapped the reads to the human genome and analyzed the reads that overlapped a diagnostic position. In total, three organoids were initially seeded as chimeric in a pilot common garden experiment, but resulted in nearly pure outcomes for one species: H1.C7B.2 had 30/33 human cells, C1.1 had 39/49 chimpanzee cells, and C1.7 had 47/47 chimpanzee cells. As such, these organoids are displayed in Figure 1 and S1 heatmaps by the dominant species. The software used in this analysis is freely available under a BSD-style license (http://www.github.com/craiglowe).

Clustering and Determining homologous cell types

Datasets underwent quality control individually, removing any cells with fewer than 1000 genes/cell, greater than 20% of reads toward mitochondrial genes, and greater than 10% of ribosomal genes. Each dataset was then normalized and scaled. Clustering of individual datasets was performed as previously described (Lefebvre, 2008); (Shekhar et al., 2016); (Nowakowski et al., 2017) using a Jaccard weighted nearest neighbor distance in the space of significant principle components followed by Louvain clustering. Homologous cell types were generated using canonical correlation analysis (CCA) (Butler et al., 2018). CCA was performed in the space of 20 correlated dimensions, and tSNE was run in the space of the CCA dimensionality reduction for visualization. Clustering of combined datasets was then performed using the Louvain-Jaccard method in the space of CCA dimensions. We also developed an alternative approach to co-cluster cells across model system or species that involved minimal transformation using a restricted set of marker genes for analysis. We first performed Louvain clustering using Jaccard distance on each dataset separately, as described above. We next selected the top 40 positive markers for each cluster from each dataset based on average difference. We then used a general linear model to remove markers with a high variance explained (typically greater than 0.1% to 1%) by model system or species, modeling these parameters as fixed effects. We then performed clustering of the combined dataset, scaled and normalized together, in the space of these restricted marker genes. This approach did not fully remove batch effects, but also retained cell subtype nuances from the original clustering and provided an independent validation of cell types as determined by CCA. Visualizations were performed in either tSNE space or using violin plots that reflected the $\log_2$(counts per million) value of gene expression.

Determining co-expression modules

WGCNA was performed using the top 2000-5000 PCA loading genes ranked across significant PCs based on absolute value of rotation scores using the WGCNA R package (Langfelder and Horvath, 2008). Parameters such as softPower, deepSplit, and cuttreeDynamic were determined independently for each dataset. To identify homologous modules from independent datasets, we used gene coexpression module kME scores across all genes to correlate modules derived from different datasets. Gene network maps presented are based on Pearson's correlation of expression levels of genes from each module, as specified in each figure legend.

Differential expression and enrichment analysis

Correlation analysis of networks to cell, species or protocol identity was performed by binarization of the variable of interest and using a Pearson's correlation to quantify the similarity across the dataset. When a correlation was performed across two cell types or other defined variables across the axis, only this set of cells was used, otherwise the whole dataset was utilized. Differential expression analysis at the gene level was performed using the likelihood ratio test and with a binary distribution suited to zero inflated data. In order to be considered as a differentially expressed gene, the average fold change was required to exceed an absolute value of $\log_2(0.25)$ and the frequency of expression was required to be greater than 25% across cells in at least one dataset. For determining genes differentially expressed during cortical development, we focused just on FOXG1+ organoids when focusing on telencephalic cell types. For each pairwise comparison, we used a general linear mixed model through the variance partition package (Hoffman and Schadt, 2016) to evaluate the extent to which fixed effects of cell type, donor, and species or protocol explain variation in each co-expression network. In all three pairwise comparisons, the majority of networks that could be explained by these

factors related to cell type, with donorID, protocol, and species, explaining substantial variation in a smaller set of co-expression modules. Enrichment analysis for module signaling pathways was performed by intersecting gene lists with curated pathways in Enrichr (Chen et al., 2013). Adjusted p values from this analysis are represented by –$\log_{10}$(p value) in histograms.

Western blots

Protein was isolated using modified RIPA buffer (Millipore Sigma) with protease inhibitor cocktail (Millipore Sigma) and PhosStop phosphate inhibitor (Millipore Sigma). Dissociated pellets of human or macaque cells, or week 5 organoids were resuspended in RIPA and vortexed. The lysate was incubated on ice for 30 minutes, after which lysates were spun for 10 minutes at 10,000 x g to eliminate debris. The supernatant protein was quantified using Pierce BCA Protein Assay Kit (Thermo Scientific). 50 ug of primary cell protein and 25 ug of organoid protein was loaded with 4X LDS loading dye plus 10% β-mercaptoethanol on a gradient 4 – 15% gel (Mini Protean TGX, BioRad) in MOPS SDS buffer (Thermo Scientific). Wet transfers were performed with transfer buffer (Thermo Scientific) with 20% methanol. Blocking and antibody incubation was perfomed in Odyssey Blocking Buffer (Li-Cor). Washes were performed with PBS plus 0.1% Tween-20. Primary antibodies (pS6 [Cell Signaling Technology; 2211], pNRDG1 [Cell Signaling Technology, 5482], p4EBP1 [Cell Signaling Technology, 2855], INSR [Novus, NBP2-12793], β-tubulin [Millipore Sigma, A1978], all 1:1000) were incubated overnight a 4°C, and secondary antibodies were incubated for 45 minutes at room temperature. Species specific IgG LT antibodies (Li-Cor) were used at 1:10000. IRDye 680 or 800 secondary antibodies were used. Scanning was perfomed using the Li-Cor Odyssey software and quantification was performed using Image Studio Lite, signal/area for each band. This signal was normalized to β-tubulin for each comparison and fold changes were calculated for each pair of samples run on the same blot (n = 3 for each species, for each primary and organoid comparisons). All antibodies were verified to bind to conserved epitopes between species.

QUANTIFICATION AND STATISTICAL ANALYSIS

Quantification of images was performed using the Imaris Image Analysis software (Bitplane). Western blot quantification was performed using the Image Studio analysis suite (Li-Cor). Statistical analysis was performed using either Microsoft Excel or Prism (GraphPad). Statistical tests, significance values, and experimental n are included in figure legends.

DATA AND SOFTWARE AVAILABILITY

The sequencing data have been deposited in GEO under ID code GEO: GSE124299 and dbGaP phs000989.v3.
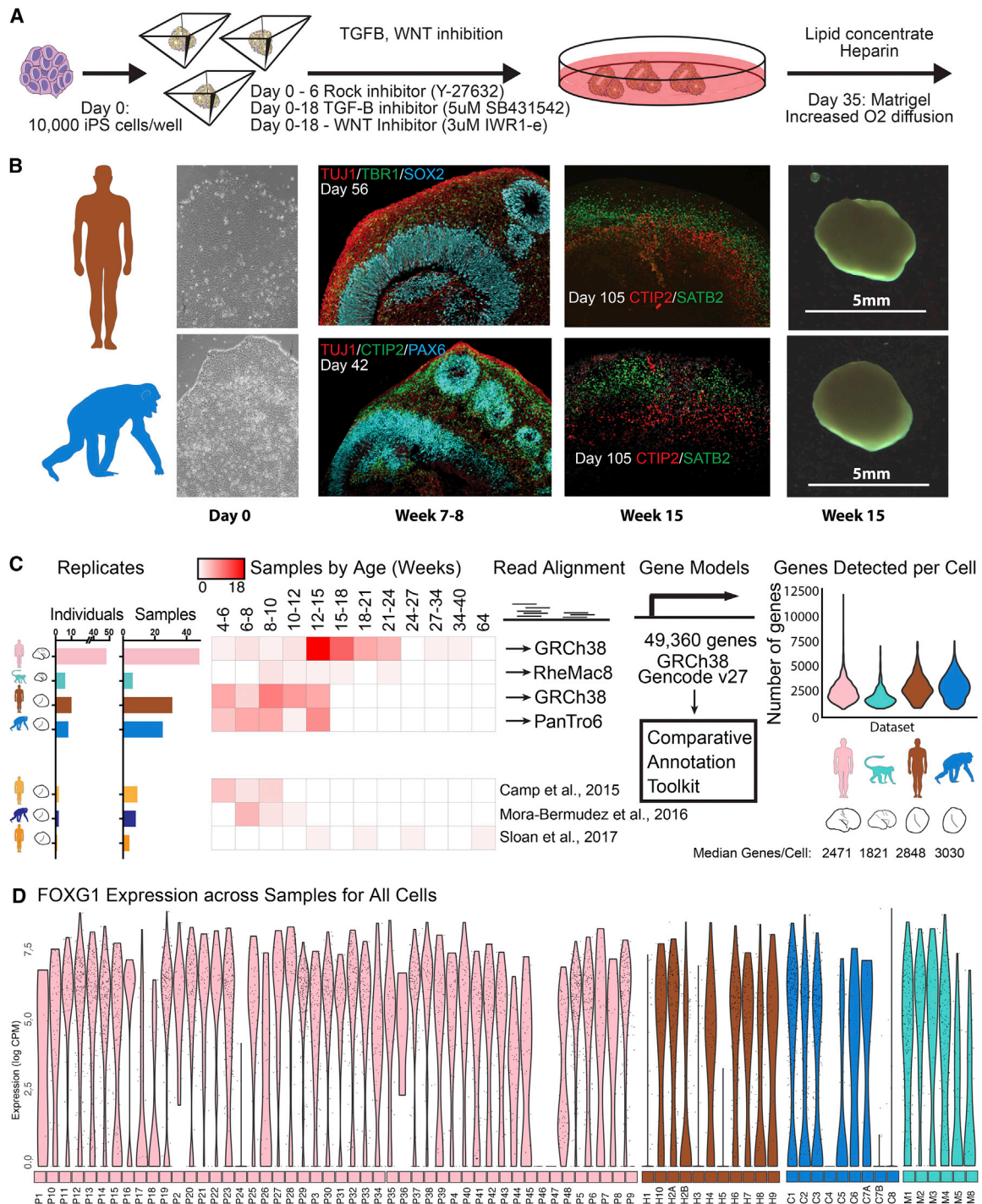
Figure S1. Study Design, Including Organoid Differentiation Protocol, Age Distribution of Samples, Alignment Methods, and Telencephalon Identity of Samples, Related to Figure 1

(A) Schematic of Kadoshima et al., 2013 protocol used in this study, including patterning molecules. This protocol represents an intermediate point between unguided cerebral organoid formation and patterning with dual SMAD inhibition.

(B) After seven weeks, human and chimpanzee cerebral organoids contain a mixture of elongated and small rosettes and express radial glia proteins along ventricular zone-like structures. By 15 weeks organoids contain neurons expressing markers of subcortically- and intracortically-projecting excitatory neurons and reach maximum diameters of up to 5mm.

(C) Histograms and heatmap depict the number of individuals and primary or organoid samples and the distribution of samples over post conception or post differentiation weeks. Human cortical neurogenesis mainly occurs from week 10 to 24, while macaque cortical neurogenesis mainly occurs from week 7 to 15.

(legend continued on next page)

Top row summarizes samples from Nowakowski et al., 2017, the next three rows describe new samples generated from the same protocol in the same conditions and laboratory for this study, and the bottom three rows summarize samples generated in previous studies in other laboratories by the same Fluidigm cell capture technology (Camp et al., 2015; Mora-Bermúdez et al., 2016) and by capturing single cells in wells but using similar reverse transcription chemistry (Sloan et al., 2017). For all datasets, reads were aligned to each species' native genome using a common set of 49,360 gene models across all three species determined with the comparative annotation toolkit (Fiddes et al., 2018). Violin plots depict the distribution of genes detected for single cells from each dataset with the median number listed below.

(D) Violin plots reflect distribution of gene expression levels for the telencephalon marker FOXG1 across primary and organoid individuals. A few individuals drive the lower efficiency of overall FOXG1+ organoids. For example, 4/5 organoids from individual H1 and 4/4 organoids from individual H5 were off target. Of the remaining 8 human individuals, 18/22 organoids were on target for telencephalon. Each dot corresponds to a single cell.
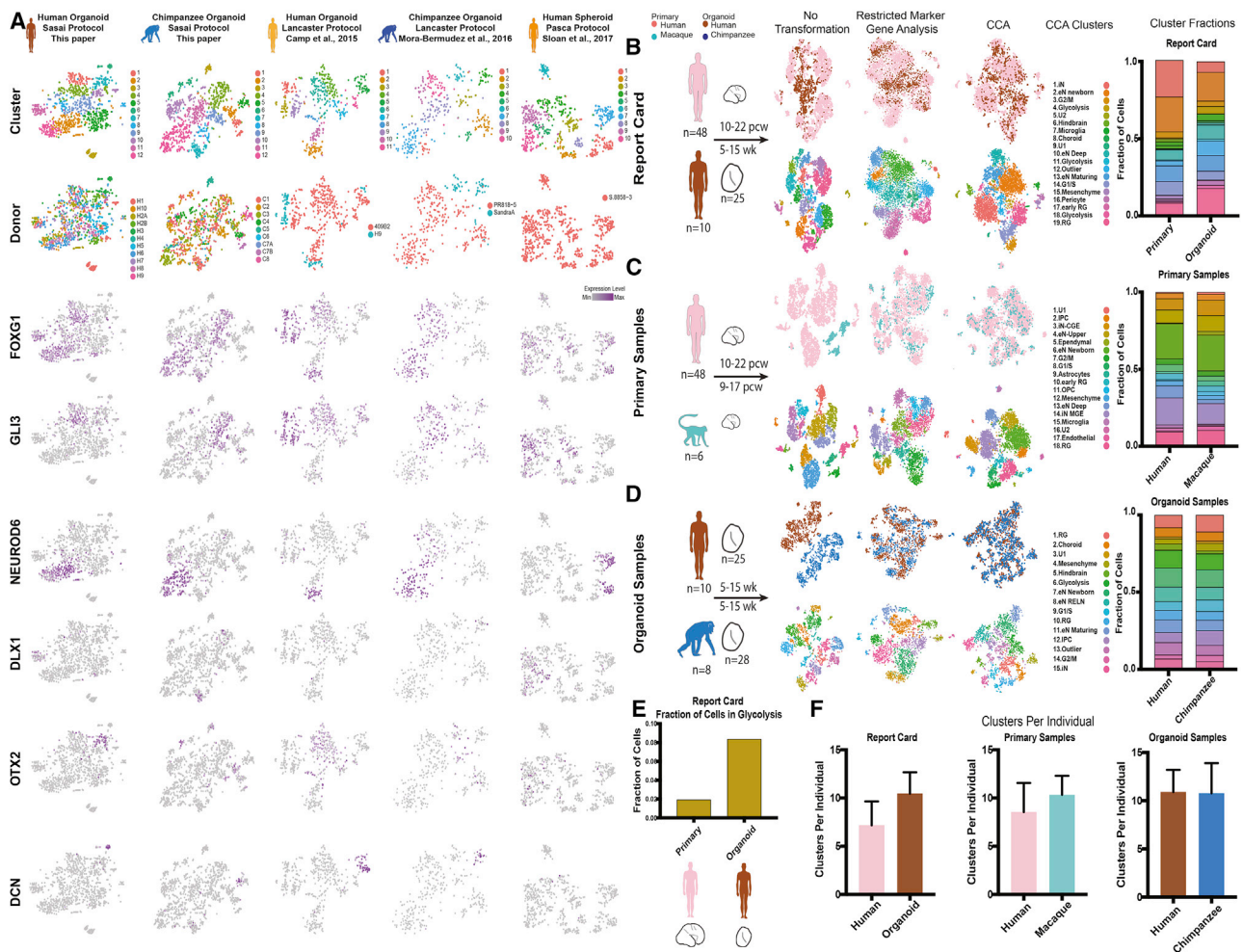
Figure S2. Clustering Analysis of Individual Organoid Dataset and Pairwise Comparisons, Related to Figure 2

(A) Organoid clusters are reproducible across individuals and represent common forebrain lineages. Five columns plot single cells from each organoid dataset in two dimensional space using t-stochastic neighbor embedding of significant principle components. Row 1 highlights single cell cluster membership for cells from this paper and previous studies. Analysis was performed through a common alignment pipeline (alignment to species' native genome, GRCh38 GENCODE v27, comparative annotation toolkit for chimpanzee) and a common clustering method (Louvain clustering of significant principle components by Jaccard distance). Row 2 colors cells by donor ID, indicating that most clusters in this study contain cells from many individuals, while previous studies contained few individuals. The next six rows color cells according to the expression of marker genes for telencephalon regional identity (*FOXG1*), radial glia (*GLI3*), cortical excitatory neurons (*NEUROD6*), inhibitory neurons (*DLX1*), ventral telencephalon, choroid plexus, and diencephalon (*OTX2*), and mesenchyme (*DCN*). All five datasets contain cortical excitatory lineages, as well as cells from other lineages, which can be distinguished by single cell RNA sequencing.

(B–D) Pairwise comparison of cells from primary human and human organoid (b), primary human and primary macaque (c), and human and chimpanzee organoids (d), with the number of distinct individuals and organoids depicted under schematic. Column 1: Clustering cells without any transformation reveals a strong species and protocol effect limiting co-clustering across batches. For example, between human and macaque primary cells, only microglia co-cluster. Column 2: Co-clustering involving a restricted set of marker genes that lack strong batch differences but with no additional transformation increases co-clustering across species and preserves cell subtype distinctions, but still yields a strong batch effect between primary cells and organoids. Column 3: Transformation of data using canonical correlation component values overcomes both species and protocol batch effects. Column 4: Cluster fractions for each comparative dataset are shown for each individual dataset.

(E) Histogram depicts the proportion of cells that fall into glycolysis clusters for each human primary and human organoid datasets.

(F) Histograms show the average number of clusters that individuals from primary samples and from organoids contribute to across the pairwise comparisons. Error bars represent standard deviation.
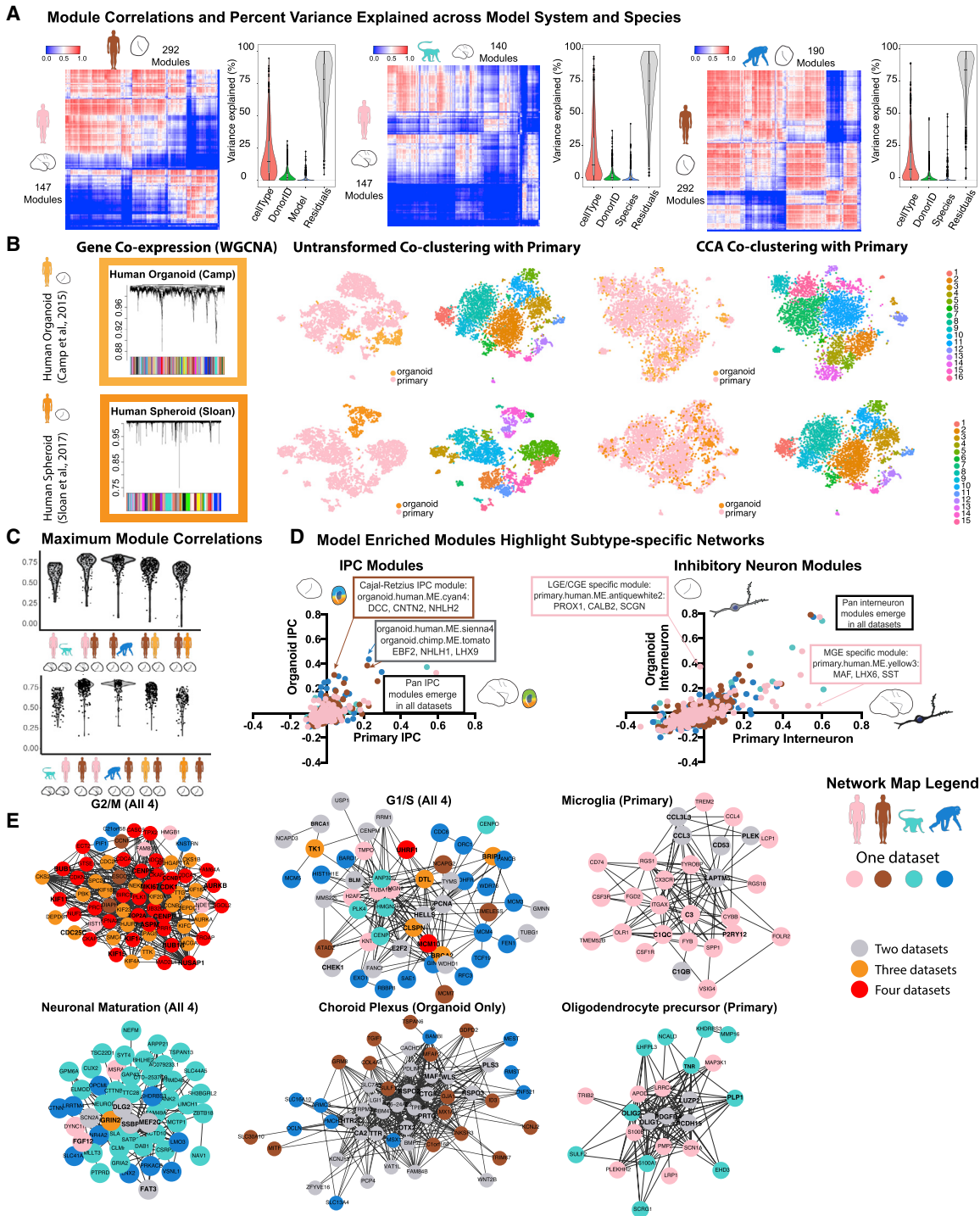
Figure S3. Gene Co-expression Modules Are Preserved across Model Systems and Organoid Protocols and Conserved across Species, Relating to Cell Type and Cell State, Related to Figure 3

(A) Heatmaps illustrate the pairwise correlation values for eigengenes representing each co-expression module across datasets, and violin plots show the distribution of the percent of variance that cell type, individual, model system or species explain in each module.

(B) We further analyzed gene co-expression networks and cluster membership for the Camp et al., 2015 dataset that used the Lancaster et al., 2013 protocol and the Sloan et al., 2017 dataset that used the Pasca spheroid protocol. Dendrogram indicates co-expression modules determined separately in each dataset across 5000 strongly-loading PCA genes. tSNE plots depict results of co-clustering organoid cells with primary cells from Nowakowski et al., 2017 without transformation and after transformation along canonical correlation components.
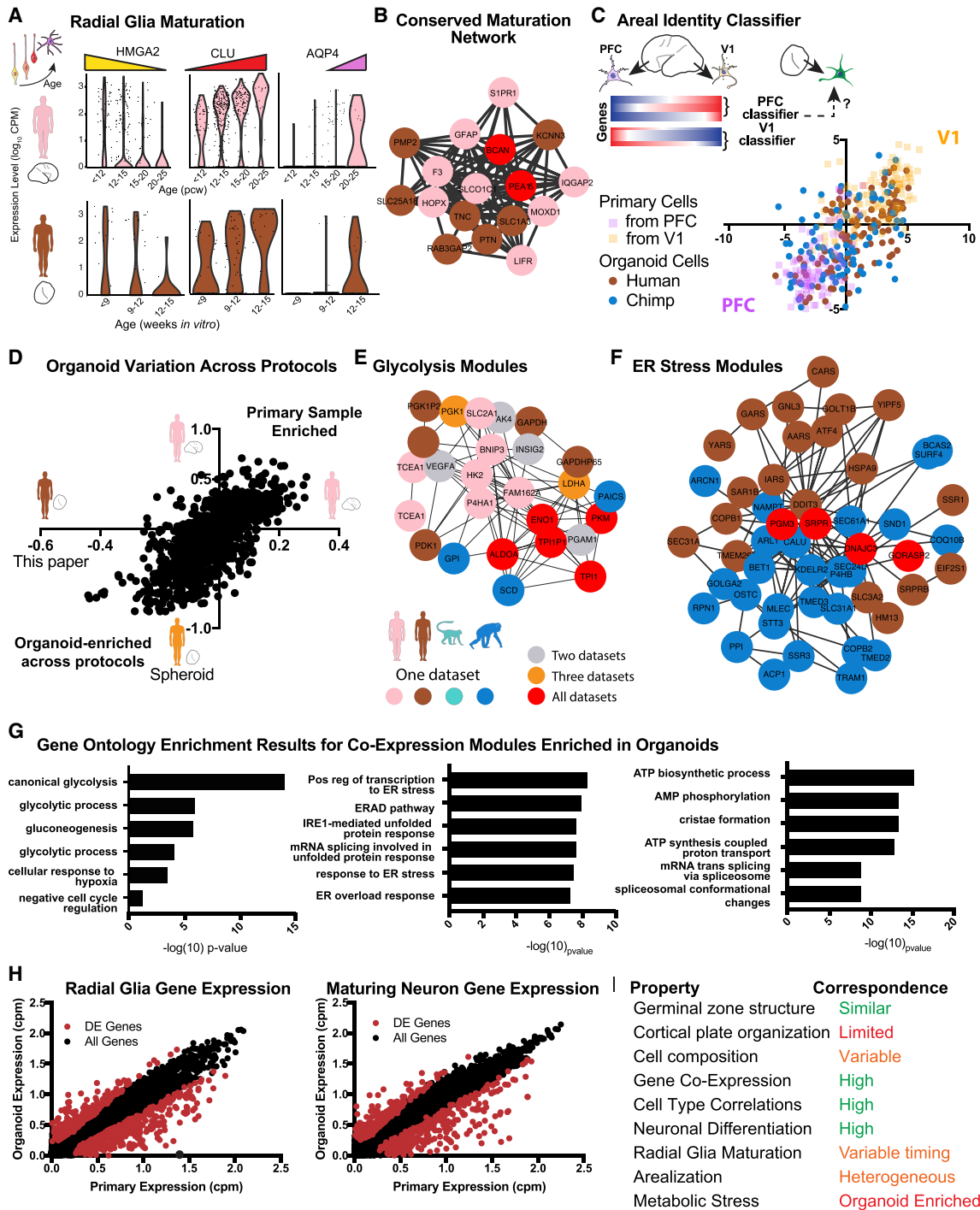
(legend continued on next page)

(C) Violin plots indicate the distribution of maximum correlation values for all co-expression modules in each pairwise comparison, using modules from the first dataset listed on the x axis, compared to the second dataset for each plot. In addition, the fourth and fifth violin plot show correlation values between human cells from our dataset (Kadoshima protocol) and the Lancaster protocol (light orange) and the spheroid protocol (dark orange).

(D) IPC and Interneuron module plots from Figure 3 are annotated to highlight modules that are more strongly correlated to the organoid or primary cell types respectively. In the IPCs, pan-IPC modules emerge in all datasets, but organoid.human.ME.cyan4 contains genes that are related to Cajal-Retzius identity, including DCC, CNTN2, and NHLH2. This module, and the two others highlighted containing EBF2, NHLH1, and LHX9, suggests a subset of both human and chimpanzee organoid IPCs may represent an earlier maturation state giving rise to the early born Cajal-Retzius neurons. Similarly, all four datasets generate very closely related and highly correlated pan-interneuron modules. However, the MGE specific module primary.human.ME.yellow3 which contains MGE specific genes MAF, LHX6, and SST is more highly correlated to primary MGE-derived interneurons on the x axis. In contrast, the module primary.human.ME.antiquewhite2 which contains CGE/LGE genes PROX1, CALB2, and SCGN is more highly correlated with organoid interneurons (y axis), as well as with CGE-derived primary interneurons (Table S4).

(E) Additional consensus co-expression modules represent cell states shared by all four datasets and cell types sampled by either organoid or primary datasets that are conserved across species. Genes are colored by the dataset in which the gene fell into the core module for the process. In these plots, each gene is colored by the dataset in which the gene appeared as a member of the core module, but the high correlation across datasets (edges represent a correlation of at least 0.15 [G1/S, OPC], 0.25 [choroid], 0.35 [G2/M] or 0.75 [microglia]) indicates conservation of co-expression relationships, and gray, orange and red dots highlight genes that appear in the core module for 2, 3 and 4 networks respectively.

A Radial Glia Maturation

B Conserved Maturation Network

C Areal Identity Classifier

D Organoid Variation Across Protocols

E Glycolysis Modules

F ER Stress Modules

G Gene Ontology Enrichment Results for Co-Expression Modules Enriched in Organoids

H

Radial Glia Gene Expression

Maturing Neuron Gene Expression

Property	Correspondence
Germinal zone structure	Similar
Cortical plate organization	Limited
Cell composition	Variable
Gene Co-Expression	High
Cell Type Correlations	High
Neuronal Differentiation	High
Radial Glia Maturation	Variable timing
Arealization	Heterogeneous
Metabolic Stress	Organoid Enriched

Figure S4. Organoid Modules Recapitulate Developmental Gene Expression Trajectories but Exhibit Elevated Metabolic Stress across Protocols, Related to Figure 4

(A) Violin plots highlight the distribution of gene expression values in primary radial glia and organoid radial glia for genes correlated with radial glia maturation during normal cortical development. Some genes like *HMGA2* and *CLU* follow expected trajectories *in vitro*, and astrocytes, as marked by *AQP4*, only appeared in the oldest primary and organoid samples.

(B) Network map shows a core radial glia maturation module is preserved in organoids, with edges representing a correlation between genes R > 0.15.

(C) Scatterplot displays maturing excitatory neurons (the *MEF2C+*, *SNAP25+* subset of *NEUROD6+* and *SLA+* excitatory neurons) from each dataset along the classifier for V1 (y axis, positive is V1-predicted) and along the classifier for PFC (x axis, negative is PFC predicted).

(legend continued on next page)

(D) Scatterplot shows the correlation of all gene co-expression networks to primary human cells (positive on both axes) versus organoid cells from this paper using the Kadoshima et al., 2013 protocol (negative on x axis) and a recent paper over a longer time course using a cortical spheroid protocol (Sloan et al., 2017; negative on y axis).
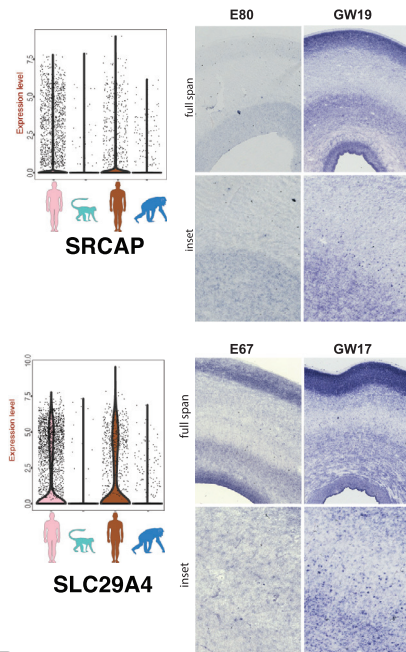
(E and F) Network maps depict the correlation of glycolysis (e) and ER-stress genes (f) across datasets with edges representing a correlation R > 0.25.

(G) Gene ontology enrichment scores for modules with the strongest enrichment in organoid models.

(H) Scatterplot shows the expression of all genes in homologous organoid and primary cell types [R^2 > 0.95].

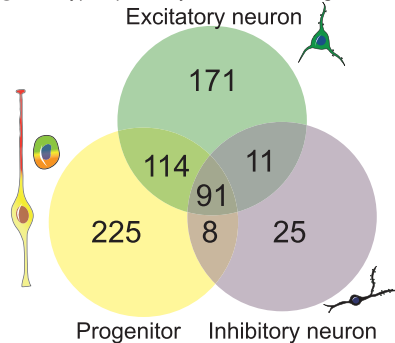(I) Summary of correspondence between primary and organoid cells across a range of metrics.
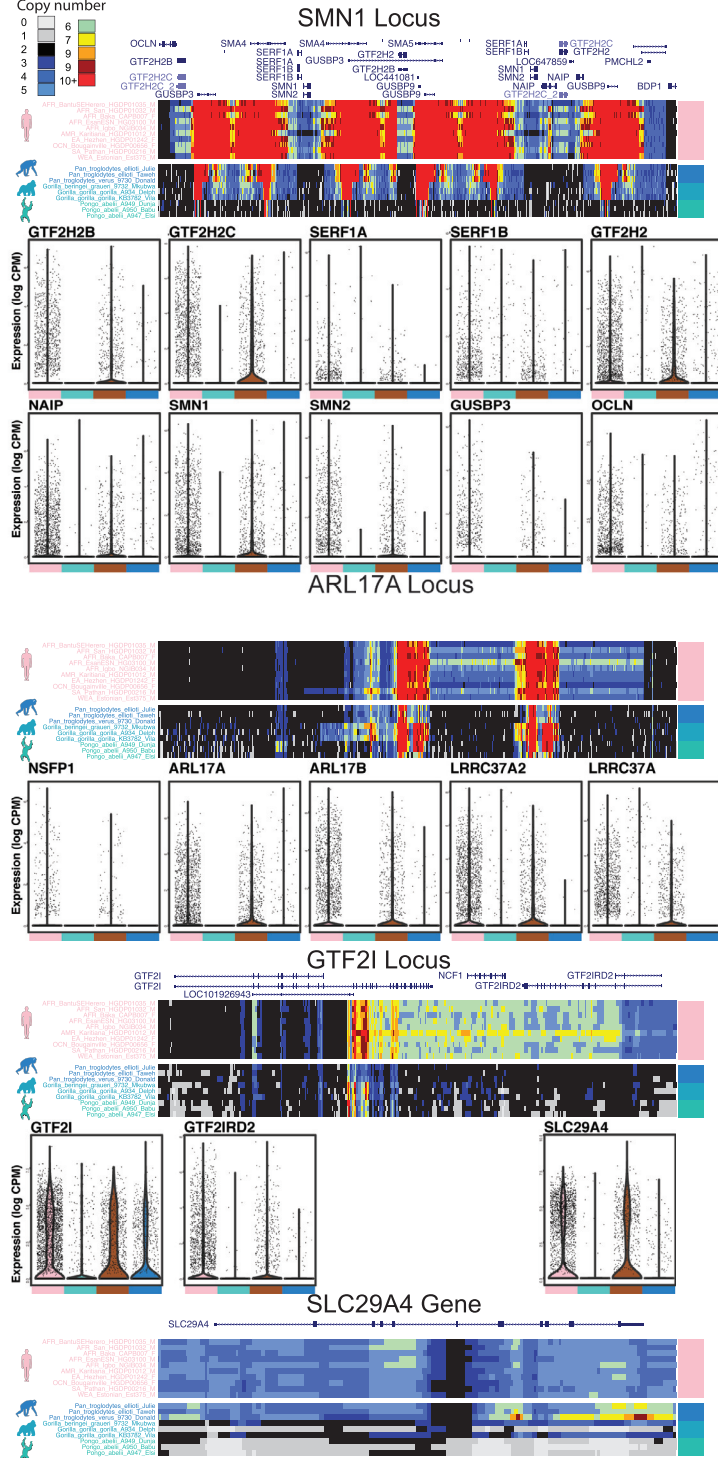
A *In situ* validation of differential expression

SRCAP

SLC29A4

B Derived changes calculated by cell type

1399 343 534

1195 387 525

889 218 540

576 135 251
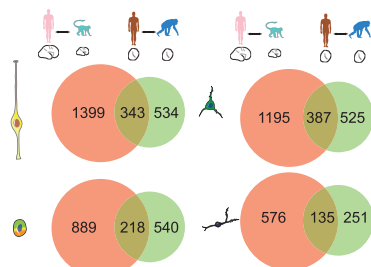
C Cell-type-specificity of derived changes

Excitatory neuron

171

114 11

91

225 8 25

Progenitor   Inhibitory neuron

D Examples of overlap of derived genes with copy number variation

Copy number

SMN1 Locus

GTF2H2B GTF2H2C SERF1A SERF1B GTF2H2

NAIP SMN1 SMN2 GUSBP3 OCLN

ARL17A Locus

NSFP1 ARL17A ARL17B LRRC37A2 LRRC37A

GTF2I Locus

GTF2I GTF2IRD2 SLC29A4

SLC29A4 Gene

Figure S5. Human-Specific Gene Expression Differences across Cell Types, Related to Figure 5

(A) Images of *in situ* hybridization performed in macaque and human primary sections for differentially expressed genes *SRCAP* and *SLC29A4*. Representative images are shown (n = 3 individuals of each species), and each show higher and more specific signal in the human than the macaque. Probes were designed to match macaque sequence perfectly in order to be conservative in evaluating comparative expression. b) For each cell type, Venn diagrams illustrate the number of differentially expressed genes between primary human and macaque (left circle) and differentially expressed genes between human and chimpanzee organoids with cortical identity (LRT adjusted p value < 0.0005).

(B) Venn diagram illustrates the overlap between derived genes as determined in each cortical cell type. Cell type-specific genes may also trend in the same direction in other cell types without reaching significance at this stringent threshold. These concerted changes are accounted for in the derived gene analysis at the level of cortical organoids.

(C) Examples of loci that have undergone recent segmental duplications and overlap differentially expressed genes. UCSC Genome Browser snapshots (GRCh38) are shown in the context of RefSeq gene annotations, with copy number heatmap tracks displaying read-depth from Illumina sequencing across representative modern humans (n = 10) from the Human Genome Diversity Project (HGDP) cohort and nonhuman primates (n = 3 each for chimpanzee, gorilla, and orangutan). Black represents single-copy with warmer colors denoting higher copy. Generation of read-depth tracks has been described previously (Sudmant et al., 2010). Violin plots are shown for genes in these loci that exhibit a significant gene expression difference or trend toward human-specific expression gains. Each dot represents a single cell.
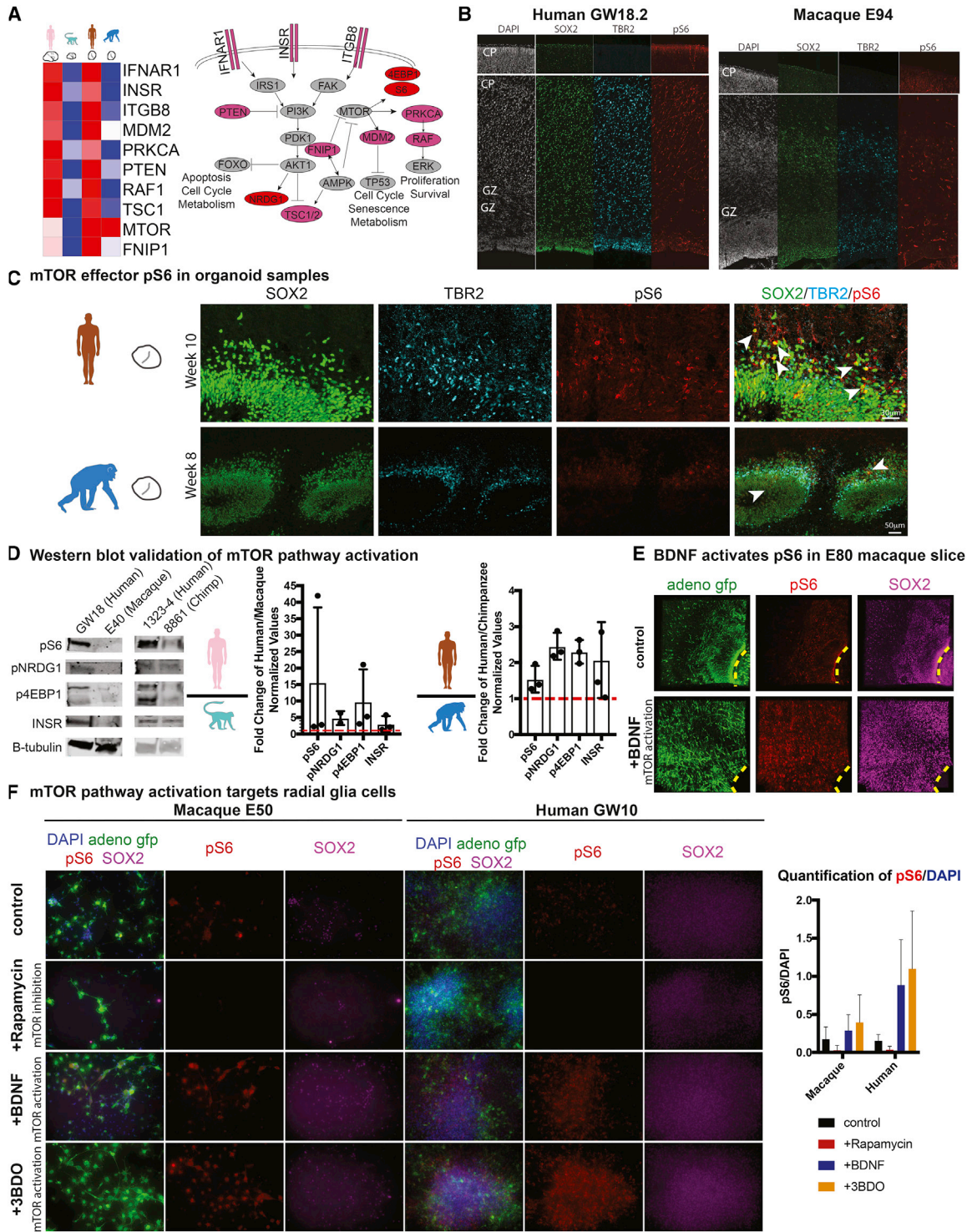
Figure S6. Human Outer Subventricular Zone Radial Glia Show Increased Phosphorylation of the mTOR Effector S6 Compared to Other Primates, Related to Figure 6

(A) Heatmap and mTOR signaling pathway diagram highlight the genes that are differentially expressed as an average across replicates. Genes highlighted in pink are upregulated in human and phosphorylated proteins downstream of pathway activation are marked in red.

(B) Immunohistochemistry of primary human outer subventircular zone shows abundant pS6 labeling in outer radial glia across biological replicates. Immunohistochemistry of primary macaque outersubventricular zone shows limited labeling of pS6 in radial glia with stronger immunoreactivity in blood vessels, while labeling in cortical plate neurons is comparable to human, supporting the efficacy of the antibody in macaque.

(C) Immunohistochemistry shows pS6 labeling in radial glia adjacent to cortical-like ventricular zones of human organoid samples which is more abundant than in the chimpanzee organoid. Arrowheads highlight example cells immunoreactive for pS6 and for SOX2. TBR2 (EOMES) labels a separate population of inter-mediate progenitors.

(D) Representative western blots are shown for human primary and macaque primary dissociated cells (E40, E50, E80 macaque, and GW10, GW16, GW18 human) as well as for human organoid and chimpanzee organoid (Week 5, n = 3 of each species). Quantifications are performed by normalization to β – tubulin levels. Fold changes were calculated for each pair of comparisons, and summary bar charts are depicted to show the relative expression of each pS6, pNRDG1, p4EBP1 and INSR. The red line demarcates the level at which comparisons would be equal.

(E) Immunohistochemistry of fibers (adeno GFP), pS6, and SOX2 (progenitors) in E80 macaque slices treated with vehicle or BDNF to activate mTOR signaling (n = 1, rare sample, paired to experiments in f). Addition of BDNF activates mTOR signal in progenitors in the macaque slice.

(F) Immunohistochemistry of GFP, pS6, and SOX2 in E50 Macaque and GW10 Human dissociated cells cultured in progenitor enriching media. Each set of dissociated cells was treated with rapamycin (mTOR inhibitor), BDNF (mTOR activation), or 3BDO (mTOR activation). Quantification of pS6 signal is shown for each condition (n = 2 for each species). mTOR activation specifically activates pS6 signaling in progenitor cells of both macaque and human.